Department of Precision and Microsystems Engineering

Hot-Formed PEEK Metamaterials: A Novel Fabrication Approach for Multi-stable Mechanical Structures

Artūras Kiselis

Report no : 2026.038
Coach : H. M. Bilyalova MSc
Professor : Dr. Ir. Marcel Tichem
Specialisation : High-Tech Engineering
Type of report : MSc Thesis
Date : 11 June 2026

Hot-Formed PEEK Metamaterials: A Novel Fabrication Approach for Multi-Stable Mechanical Structures

by

Artūras Kiselis

to obtain the degree of Master of Science
at the Delft University of Technology,
to be defended publicly on Thursday June 11, 2026 at 13:45 PM.

Student number: 6048897
Project duration: 25 April, 2025 – 11 June, 2026
Thesis committee: Dr. Ir. M. Tichem, TU Delft, supervisor
H. M. Bilyalova MSc, TU Delft

TU Delft

Preface

This thesis marks the end of my academic journey at TU Delft. These past few years have been the best of my life and I would like to express my gratitude for the guidance and support I have received. I would not have been able to reach this milestone without my family and, especially, my close friends here in Delft.

First of all, I would like to thank my supervisor, Marcel Tichem, who has provided invaluable help and support. Your charisma captured my attention from my very first day at the university, when I knew I wanted to write my thesis under your supervision. I deeply appreciate your efforts, your desire to challenge and the opportunity to gain invaluable knowledge in microengineering

I would also like to express my thanks to my daily supervisor, Hava Bilyalova, for helping me navigate daily challenges and providing support throughout the project. You really motivated and helped me push forward during this research.

My sincere appreciation goes to the people who have been around me, you made my time in Delft an unforgettable experience. I would like to thank my football team for the amazing time and for reigniting my love for the sport. I cannot thank Lucas, Justas, Ingi, and Doddi enough for being there for me, especially during the first half of my studies and I really hope our friendship will last a lifetime. I would also like to express my utmost appreciation to Doddi - I don't think I would have been able to reach this stage without your support, thank you. Also, my special thanks go to my Icelandic friends for their warm attitude and for always making me feel welcome.

Finally, I would like to express my gratitude to my family for their unwavering support and for always believing in my academic endeavours.

Artūras Kiselis
Delft, May 2026

Contents

1 INTRODUCTION **1**
- 1.1 Research Background . . . 2
- 1.2 Objective . . . 2

2 MATERIALS & METHODS **2**
- 2.1 Geometric design . . . 2
  - 2.1.1 Bistable unit cell design . . . 2
  - 2.1.2 Row deformation sequence . . . 3
  - 2.1.3 Material selection . . . 3
- 2.2 Fabrication . . . 3
  - 2.2.1 Laser processing . . . 3
  - 2.2.2 Mould fabrication workflow . . . 3
  - 2.2.3 Hot forming . . . 4
  - 2.2.4 Assembly . . . 5
- 2.3 Microscopic measurements . . . 5
- 2.4 Numerical analysis . . . 5
  - 2.4.1 Mesh study . . . 5
- 2.5 Experimental validation . . . 6

3 RESULTS AND DISCUSSION **6**
- 3.1 Fabrication . . . 6
  - 3.1.1 Mould dimensional accuracy . . . 6
  - 3.1.2 Effects of hot-forming duration . . . 6
  - 3.1.3 Unit cell stress state . . . 7
- 3.2 Single beam unit cell . . . 7
  - 3.2.1 Design . . . 7
  - 3.2.2 Local geometric tailoring . . . 8
- 3.3 Triple beam unit cell . . . 8
  - 3.3.1 Design . . . 8
  - 3.3.2 Parametric study . . . 9
  - 3.3.3 Scalability . . . 10
  - 3.3.4 Multi-cell lattice . . . 10
  - 3.3.5 Multilayered structure . . . 11
  - 3.3.6 Deterministic deformation . . . 11
  - 3.3.7 Rotational compliance . . . 12
- 3.4 Process limitations . . . 13

4 CONCLUSIONS AND FUTURE WORK **14**
- 4.1 Conclusions . . . 14
- 4.2 Future work . . . 14

A Tables **16**
- A.1 FEA mesh study parameters
- A.2 Effects of hot forming duration
- A.3 OPTEC laser parameters
- A.4 Substrate thickness influence on maximum and minimum force

B Figures **17**
- B.1 Mould general dimensions
- B.2 Mould surface and geometry
- B.3 Unit cell test bed assy
- B.4 Scaled unit cells
- B.5 L1H05 Unit cell
- B.6 Thermally fused moulds
- B.7 Assembly arrangement
- B.8 Multi-stable system test setup
- B.9 Plotted *F-d* response at 50µm thickness

C Metamaterial fabrication process **21**

D PEEK sheets APTIV FILMS 1000 **22**

E Matlab code **23**

F Literature review **26**

G Literature review **27**

Hot-Formed PEEK Metamaterials: A Novel Fabrication Approach for Multi-stable Mechanical Structures

Arturas Kiselis

Department of Precision and Microsystems Engineering
Delft University of Technology
Mekelweg 2, 2628CD, Delft, The Netherlands

Abstract

Multi-stable mechanical metamaterials, composed of bistable unit cells, exhibit multiple equilibrium states and maintain either configuration without continuous external actuation. Despite unique functionality, their integration into high-precision motion systems remains constrained by the limitations of conventional 3D fabrication techniques. This thesis utilises the MECOMOS (Mechanical Metamaterials for Compact Motion Systems) manufacturing platform to develop a novel multi-stable mechanical metamaterial. The proposed methodology employs a hot-forming technique to form 100 µm and 200 µm PEEK substrates into functional, millimeter scale bi-stable unit cells which are subsequently assembled to form a 3D homogeneous metastructure. The findings of this study are categorised into three primary stages: fabrication process optimisation, the unit cell design architecture and the functional performance of the assembled metastructure. Evaluation of the fabrication process was conducted through analysis of the dimensional stability of the SLA printed moulds and the hot forming parameters, revealing the necessity of a sufficient forming duration. Initial investigations into the unit cell geometry utilised a single cosine beam configuration, identifying the fundamental requirements for bistability: the geometric profile of the beam and the effective stiffness of the surrounding boundaries. Subsequent development of the three-dimensional (3D) unit cell, characterised via Finite Element Analysis (FEA) and quasi-static experiments, demonstrated a high sensitivity to geometric variations via the force-displacement response with peak forces remaining below 1 N. Concurrently, the structural limits of the fabrication process established a minimum achievable beam feature size of 500 µm. By arranging these 3D unit cells into a honeycomb lattice, the multi-stable functionality of the metamaterial was validated through deterministic row displacement and the tilt compliance of the multi-cell layers. Collectively, these results demonstrate the viability of replication-based fabrication for achieving tunable, millimeter scale multi-stable metamaterials suitable for precision motion components.

Keywords: Bistable mechanisms, multistable metastructure, PEEK mechanical metamaterials, hot-formed mechanical metamaterials, snap-through.

1. INTRODUCTION

The development of metamaterials has been driven by the need for enhanced mechanical functionality beyond the capabilities of conventional materials [1]. Their unique properties are driven by geometric design of periodically arranged building blocks, commonly referred to as unit cells. A particular subgroup of mechanical metastructures, called negative stiffness metamaterials, demonstrate unique phenomenon where an increase in deformation of a structure or material results in a decrease in load [2]. This results in a non-linear snap-through transition in the structure demonstrating two distinct equilibrium states called bistability. Most of the research on bistable mechanical metamaterials display level (stable) translational deformations and limited functionality, focusing mostly on energy absorption, vibration isolation or shape reconfiguration due to absence of rotational compliance within the unit cell's structure. Recent studies have introduced a novel approach to 3D unit cell design in which the structure exhibits both level and tilted stable configurations enabling new opportunities for motion system design [3] as shown in Figure 1.1. Therefore, these mechanical structures can introduce a significant reduction in volume and complexity needed in high-tech motion systems. However, the vast majority of currently found metastructures in the literature are not suitable for microscale applications in precision engineering and thus, demand alternative approach to metamaterial fabrication.

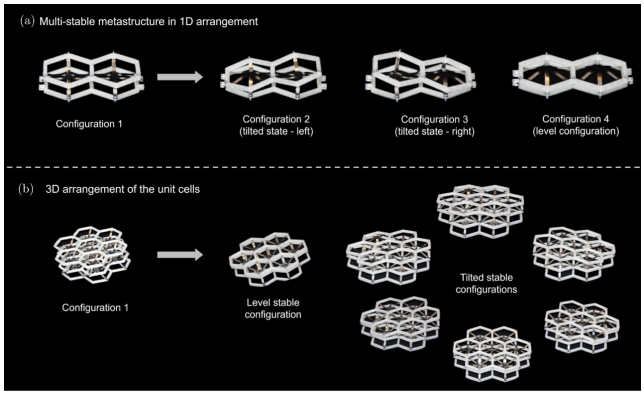

Fig. 1.1. A multi-stable metastructure showing level and tilted stable configurations [3].

1.1. Research Background

To further advance negative stiffness mechanical structures within micro and nano industry, an alternative high fidelity and high throughput manufacture method is required. Some studies indicate that relatively small metamaterials can be achieved using the FDM (Fused Deposition Modeling) [4] or SLS (Selective Laser Sintering) [5] fabrication methods. However, although widely used and well developed, their subcentimeter capacity is limited. On the other hand, high-fidelity functional submillimeter scale multi-stable metastructures were fabricated using the 2PP (Two-Photon Polymerisation) method [6]. Despite such innovation, this presents engineering challenge at a high cost of manufacturing time and resources. Thus, evidently, a method for subcentimeter metamaterials at relatively high production output is needed.

A research project - Mechanical Metamaterials for Compact Motion Systems (MECOMOS) developed at TU Delft focuses on methods for design and manufacture of 3D micro mechanical metastructures [7]. The MECOMOS process involves replication-based manufacturing of thin sheets in such way that stacking multiple formed substrates results in complex motion functionality, like complex multi-directional kinematics, actuation, transmission, and multi-stability. Previous work within this framework investigated hot forming capacity of polymeric substrates and its limits whilst evaluating feasibility for implementation in submillimeter homogeneous metamaterial structures [8]. Findings of the study presented the smallest repeatable microscale features which measured $400\times400\times100\,\mu m$ in size enabling high fidelity fabrication with relatively high accuracy. Therefore, with promising hot forming results and broad range of process parameters, the foundation for the novel fabrication method of precise multi-stable metastructures was set.

1.2. Objective

Building upon the foundational research of Zhang et al. [3] and M. Rings [8], this paper addresses existing constraints by refining a novel methodology and integrating multiple processes for the production of microscale multi-stable mechanical metamaterials. The first instance of design and characterisation of hot-formed metastructures using PEEK is presented. By utilising and optimising upon the fabrication process, the study demonstrates concept feasibility and contributes to the broader MECOMOS project.

This thesis is organised into four primary sections. The section 2 details the design, fabrication, and methodology for the proposed unit cell and resulting metastructure. This section first establishes the theoretical framework for the design choices before detailing the fabrication techniques and critical assembly steps required to achieve a multi-stable mechanical metamaterial. Furthermore, the thesis methodology including microscopic characterisation, numerical analysis and experimental validation is presented. The section 3 provides a comprehensive discussion of the fabrication outcomes, evaluating single beam unit cell design and the 3D unit cell configuration that forms the core of this research. Results of the unit cell characterisation will be covered with various design modifications for improved performance,revealing a final multi-stable mechanism. This section also addresses encountered challenges and the study's limitations. Finally, section 4 concludes findings and proposes recommendations for the future research.

2. MATERIALS & METHODS

To produce a functional bistable mechanisms using the replication-based method, a four stage fabrication process was defined as shown in Figure 2.1. Stage I starts with a mould design, printing and post-processing. The second stage is laser cutting which releases the desired shape as a 2D planar profile. The following stage is hot forming where the 2D open geometry obtains its definitive shape. At this stage, a bistable unit cell or a single cell lattice is formed. Consequently, combination of formed multiple unit cells on a single substrate results in a bistable multi-cell lattice. Finally, the last stage of the process is the assembly where lattice sheets are collated and stacked resulting in the homogeneous multi-stable mechanism. A more detailed reference of the complete process is described in Appendix C.

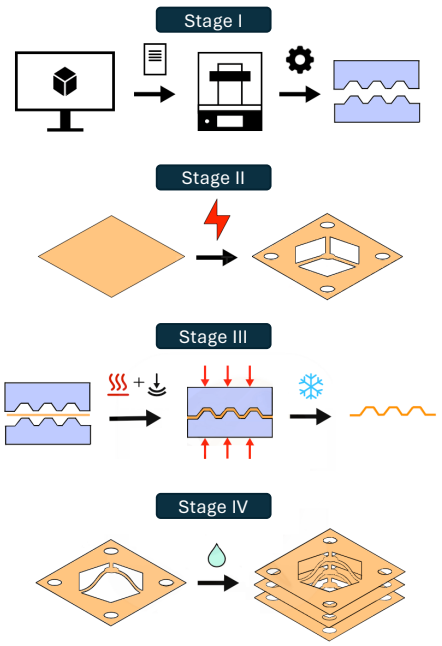

Fig. 2.1. A four stage metamaterial fabrication process diagram.

2.1. Geometric design

2.1.1. *Bistable unit cell design*

The proposed bistable unit cell design is derived from a pre-curved cosine beam which has been extensively studied in bistable beam structures [9]. The mathematic expression of the cosine beam is shown in Equation 1.

$$w(x) = h/2[1 - cos(2\pi x/l)] \tag{1}$$

Here, x represents the horizontal coordinate along the span of the beam, l. Parameters t and b are in-plane and out-of-plane thickness while h is the height of the cosine beam as shown in Figure 2.2.

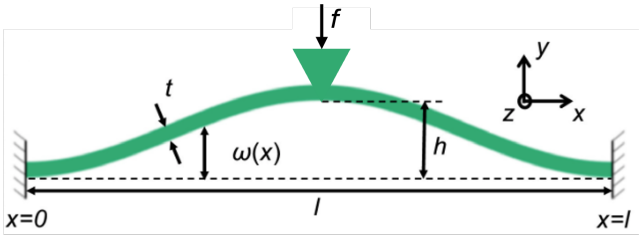

Fig. 2.2. Geometrical configuration and parameters of the cosine curved beam [10].

The geometric relationship governing the snap-through transition is determined by the factor Q, defined as:

$$Q = h/t \tag{2}$$

Specific values of Q determine stability conditions having a significant effect on the force–displacement (F-d) curve i.e, when $Q > 2.31$ the beam is bistable, while $1.21 < Q < 2.31$ exhibits a snap-through monostability. Additionally, during transition, a curved beam experiences rotation at the midpoint leading to the second buckling mode. To counteract this unwanted phenomena, it was determined that the single beam must have a centre plunger attached to increase the stiffness at the midspan and restrict undesired rotations as seen in Figure 2.2 [10]. Hence, all metamaterials based on a pre-curved beam are designed in such way that satisfies two bistability conditions: 1) large enough Q factor and 2) constrained second buckling mode. Other essential geometric parameters influencing performance of cosine beam structures are thickness-to-span ratio λ (t/l) and height-to-span ratio h/l. Both of these relations influence tuning of maximum force F_{max} during the bistable response. However, effects of t/l are significantly more influential than h/l due to variation of thickness. The amplitude of F_{max} and beam's thickness, t are closely related as it dictates the bending and axial stiffness of the cosine beam. Therefore, overall rotational stiffness is a dominant factor in stiffer mechanical response and subsequently, higher maximum force [11]. The thickness of supporting segments around the cosine beam i.e., the boundary, is also considered as one of the most important factors for the mechanical snapping mechanisms. Hence, presence of relatively thicker supports, compared to snapping beam element, results in monostability or bistability.

2.1.2. Row deformation sequence

The performance of a multi-stable metastructure within a motion system is evaluated not only by its deformation step size or F_{max} but also by its deformation sequence. While the sequence may be secondary in most energy absorption applications, it is essential for the performance of precision alignment mechanisms. The collapse order of multi-stable mechanisms is controlled via stiffness which directly correlates to the thickness of the cosine beam, t in each layer [12]. That is, once the vertical force is applied, snap-through deformation is initiated via least stiff unit cell layer where the stiffest layer is the last to deform.

Thus, combination of these parameters suggests that the bistable response is geometry dependent and mainly decoupled from the material properties of the substrate. By applying these aforementioned geometric relationships, the following sections will present multiple unit cell designs explored in this study.

2.1.3. Material selection

Polyether ether ketone (PEEK) is a high-performance organic thermoplastic material which has exceptional mechanical properties, high thermal stability and chemical resistivity which makes it ideal for high-end applications. A major advantage of PEEK is its micro scale fidelity i.e., ability to form micro scale high precision features once the glass transition temperature, T_g, of 143 °C is reached under pressure [13]. In addition, PEEK is resistant to nearly all organic and inorganic chemicals and retains stable geometry over time due to inherently high creep and fatigue resistance. Therefore, due to combination of these characteristics, PEEK was selected as an optimal material for this study, using substrate thicknesses of50 µm, 100 µm and 200 µm (Victrex, APTIV FILMS 1000 series, Appendix D).

It is worth mentioning that some experimental work was conducted with Polycarbonate (PC) to study improving the stiffness of the sheet boundary conditions. However, poor thermal bonding between the PC and PEEK layers proved insufficient due to fabrication conditions used in this study.

2.2. Fabrication

2.2.1. Laser processing

The first step in the unit cell fabrication is laser machining. First, sample processing tests were conducted using the OPTEC laser system to determine optimal processing parameters for different substrate thickness as tabulated in Table A.3. Then, once optimal laser machining parameters were established, individual PEEK sheets were precisely cut into 35×35 mm squares to match the moulds where the beam unit cell geometry was released in the center. Notably, differences in laser parameters for 200 µm sheet resulted in stronger power output and cycle count leading to a more visible heat affected area. Nonetheless, this had no effect on subsequent fabrication steps or the final performance of the unit cell.

2.2.2. Mould fabrication workflow

The mould fabrication workflow used in this study is based on earlier pre-developed methods involving SLA printing, washing, thermal curing and hot forming. Modifications were implemented in each of the processing step, however, general methodology remained unchanged to preserve mould fabrication consistency throughout the study.

Printing

The mould fabrication process applied in this study utilises polymer additive manufacturing (AM). Major advantages of the polymer AM are geometric freedom, absence of tooling costs and material customisation which enables fast prototyping at relatively low cost. On the other hand, the drawbacks of polymer AM are associated with increased cost at high-volume output, poor surface finish and labour intensive post-processing [14]. An excellent countermeasure for these drawbacks is SLA (Stereolithographic) printing, specifically developed to improve rough surface finish and loose dimensional tolerances needed for complex high-fidelity features. Therefore, a Form 3+ SLA printer (from Formlabs) was selected. To maintain the high fidelity of the printed moulds, the deposition layer height was set at h = 0.025 mm. Due to nature of the fabrication process, moulds are exposed to elevated temperatures during the hot forming thus, a high temperature resistant V2 resin was utilised to ensure thermal stability.

Overall structural features of the SLA printed positive and negative molds are shown in Figure B.1a and Figure B.1b which were modeled using the SolidWorks 2025 Computer Aided Design (CAD) software. As depicted, it contains features like alignment pins, overall dimensions, grooves (for reduced contact area with the printing base plate), and, in the center, a unit cell lattice pattern. First, the design was created for the positive mold with the unit cell architecture. Then, an extruded cut was made for the negative mold, resulting in a cavity of the desired cosine beam arrangement. This way, the accuracy and positioning errors between adjacent parts were avoided. The final printed moulds used in this work are illustrated in Figure 2.3.

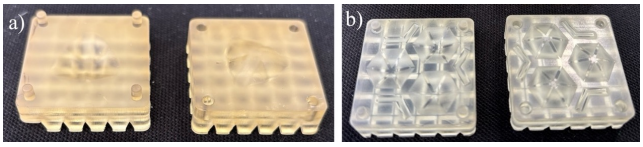

Fig. 2.3. SLA printed moulds, negative (left) and positive (right): a) For the single cell lattice, as-printed; b) For the multi-cell lattice, used.

Washing

Once the print was finished, moulds were washed to remove excess resin. The total washing procedure was divided into three stages: a primary washing stage (dirty bath), a secondary wash (clean bath) and the final rinse (for more details refer to C in the appendix). First, the platform which contains moulds, was placed into a first automated washing bath filled with isopropanol (IPA) and set for a 2-minute cycle. Once finished, the platform was removed from the first bath and inserted into a second bath for 3 minutes. Once the second washing stage was completed, moulds were detached from the platform and placed into an ultrasound washer for 3 minutes to remove the smallest debris from the moulds. To avoid IPA absorption, which can decrease mould performance during hot forming and reduce feature accuracy, moulds were washed no longer than 10 minutes in total. Finally, moulds were dried under pressurised air to ensure complete removal of IPA from the surface.

Thermal curing

The mould fabrication process concludes with thermal curing, a critical stage that ensures structural integrity and dimensional stability. This final treatment is essential for attaining the optimal mechanical properties and functionality required for multiple hot forming cycles. Just as the washing, thermal curing was completed in several stages. Once moulds were cleaned in the IPA, they were inserted into the Form Cure V1 (Formlabs) curing chamber. The initial heating was set for 2 minutes in 35 °C. Then, with controlled temperature ramp of 10 °C every 2 minutes, final temperature of 65 °C was reached allowing moulds to cure for additional 60 minutes resulting in translucent yellow colour as shown in Figure 2.3 a).

2.2.3. *Hot forming*

Once the moulds were fabricated and the sheets laser processed, hot forming was performed. Hot forming is a process that combines thermoforming and embossing to achieve high resolution features over an entire substrate. In this work, an pre-existing equipment setup was used as illustrated in Figure 2.4. The Alfamatic electric press (Italy) was modified by adding top and bottom heating elements that were heated to 150 °C for PEEK forming. This way a, parallel pressure distribution was achieved with uniform heating. To initiate the hot forming procedure, laser machined PEEK sheet was inserted into two matching positive and negative molds and placed onto the bottom heating element where controlled 1.7 kN downward pressure was applied.

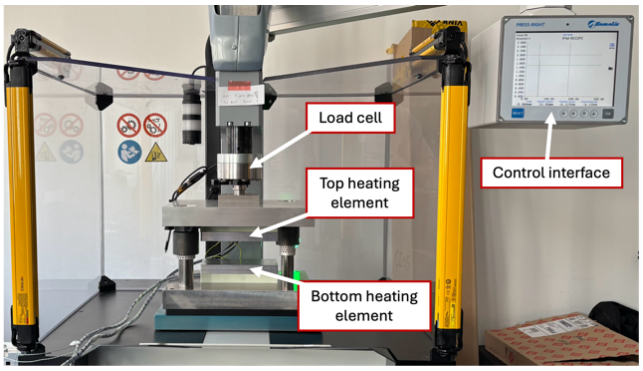

Fig. 2.4. A pre-defined thermoforming setup using the Alfamatic electric press.

The established forming duration for multiple PEEK substrates is tabulated in Table 2.1 which shows six-fold increase in forming time for subsequent increase of substrate thickness from 50 µm to 200 µm. Once enough time had passed, moulds were removed and subjected to 19.62 N (2 kg) weight at the ambient temperature. This way, the formed sheet was allowed to gradually cool down for 5 min to relieve any internal stresses and increase dimensional stability of the unit cell.

Table 2.1. The effect of thickness on hot forming time.

	50 (µm)	100 (µm)	200 (µm)
Time (s)	180	720	960

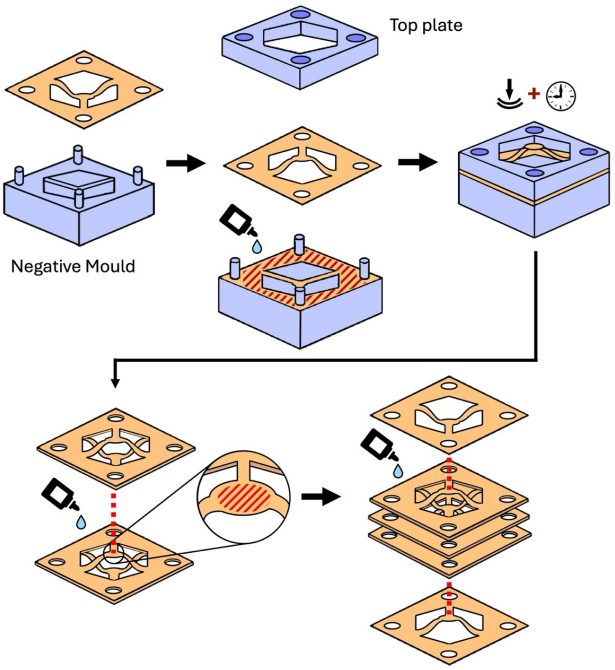

Fig. 2.5. Multi-layered metastructure assembly process diagram.

2.2.4. *Assembly*

The final phase in the fabrication of the multi-stable metastructure is the assembly process presented as a process workflow diagram shown in Figure 2.5. Although the unit cell lattices featured fine geometric features, their manual alignment remained highly effective allowing slight positioning variations without compromising precision. Cyanoacrylate, a fast acting adhesive, was used as a binding agent between the PEEK cell layers in locations depicted as a hatched area in Figure 2.5. Following the application, a curing period of 4−5 min was required to ensure a robust bond. Initially, a single layer was positioned within the negative mould, after which the cyanoacrylate was applied to a flat surface area of the unit cell. Subsequently, a second mirrored layer was placed in direct contact and consolidated using an assembly top-plate and a static weight of 19.62 N (2 kg). Once the primary bilayer consolidated, subsequent bilayers were joined at the apices of the unit cell structures creating a bistable row. To complete the multi-stable system, the top and bottom boundaries were joined using individual single layers at their midsections as shown in Figure 2.5. Using this method, uniform and varying thickness PEEK bistable lattice layers were joined together to form a multi-layer multi-stable metastrcuture with no beam deformation or alignment issues.

2.3. Microscopic measurements

Dimensional measurements of the mould features were performed using a Keyence digital microscope VHX-6000 at x20 − x50 magnification. Images were captured and analysed using the image processing software integrated within the manufacturer's equipment. Multiple measurements were taken of the moulds and substrate samples to compare against their designed features. The shape of hot-formed beams was qualitatively investigated and surface quality evaluated with the assessment of geometrical features.

2.4. Numerical analysis

To simulate snap-through transitions and capture expected forces, ABAQUS CAE (2025), a commercially available finite element model (FEM) software was used. The constituent material of the unit cell is PEEK which was assumed to be linear elastic in all simulations. Young's modulus was set at 2350 MPa. Dynamic implicit step solver was used with Nlgeom function selected for quasi-static application. The unit cell was modeled as a homogeneous continuum shell with selected Poisson's ration as 0.4 due to extremely high thickness to length ratio. The model was meshed with 4-node quadratic elements with reduced integration (S4R). The edges of the model were fully fixed, effectively eliminating any rotations and translations. Finally, displacement control loadings used in simulations were applied for the unit cell and multilayer models.

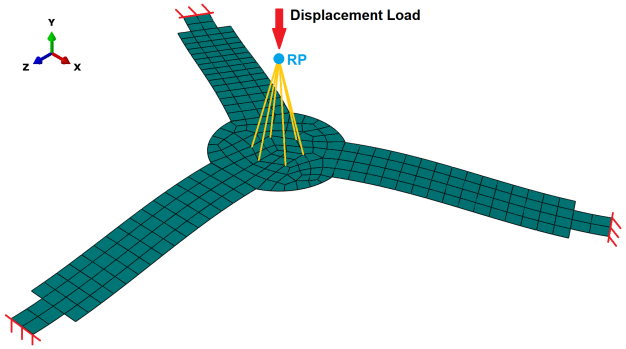

Fig. 2.6. The finite element (FE) model of the unit cell.

2.4.1. *Mesh study*

To ensure stability of obtained numerical results, the mesh sensitivity analysis was conducted. The specific parameters of the unit cell were $l = 10.0$ mm, $h = 3.0$ mm, $t = 0.20$ mm and $b = 2.0$ mm. As shown in Figure 2.7, five different global seed sizes were chosen ranging from 0.1 mm to 2.0 mm. Although the force-displacement graph converged with the element size of 0.1 mm, it is computationally expensive and time consuming to use such fine mesh grid resulting in total computation time of 430 s. Total results of the mesh convergence study are in Table A.1. Element size analysis revealed that global seed size of 2.0 mm and 1.0 mm yield unacceptable F_{max} errors at 12.42 % and 4.78 % deviation respectively. Consequently, the element size of 0.5 mm was identified as the optimal mesh density, proving a balance between accuracy and computational cost with deviations for F_{max} and F_{min} limited to 1.89 % and 3.45 % respectively. Consequently, to analyse dimensionally smaller

unit cells, mesh density of two elements per beam width is preferred.

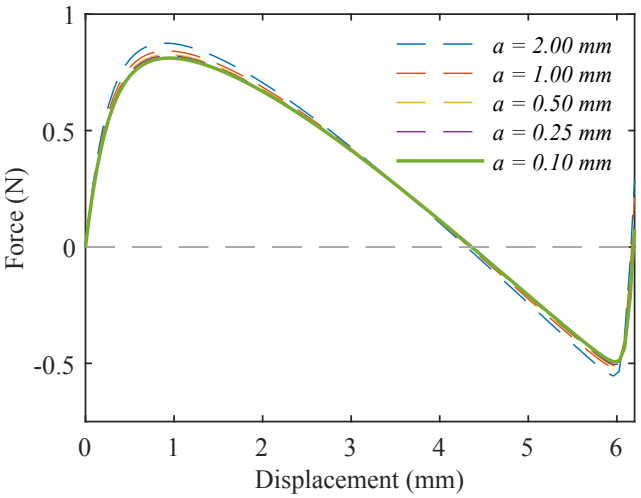

Fig. 2.7. FEA mesh study results with global seed size, a, ranging from 0.1 mm to 2.0 mm. Element type S4R.

2.5. Experimental validation

To validate numerical results and plot the $F - d$ response of the unit cell, a quasi-static test was conducted using the uniaxial testing machine (ZwickRoell Z005, Germany) where Figure 2.8 illustrates the setup. The unit cell sheet was placed into the test bed (shown in Figure B.3) to ensure rigid boundary conditions where only the cosine beam experiences the applied vertical force. The frame was then fixed on both ends by the fixtures to ensure lateral stability of the sample. To apply concentrated load, the center of a unit cell was aligned with the end point of the load cell and glued for a stiff connection point using cyanoacrylate. Then, a displacement controlled load was applied at a rate of 2 mm/min to record specimens and quantify as force-deflection curves shown in this paper. Quasi-static tests for multi-stable metastructures were conducted under similar test arrangements, however, additional top and bottom fixing plates were attached for rigid connection with the test equipment. This way, the force was applied directly through the top layer enabling unrestricted deformation of the subsequent rows. A more detailed explanation is shown in Figure B.8.

3. RESULTS AND DISCUSSION

Results presented in this section are presented in three sections. The first section presents fabrication results including mould dimensional accuracy, effects of hot-forming duration and qualitative observations of the formed substrate's stress state. The following section will cover the initial design investigation of the single beam unit cell by presenting design decisions, local geometrical modifications and the analysis of corrugations for the stiffness enhancement. The final section will examine a 3D unit cell design. This will include analysis of geometrical parameter study, scalability limits of the fabrication process, deformation and rotational compliance of the multi-stable unit cell, and finally, outline process limitations.

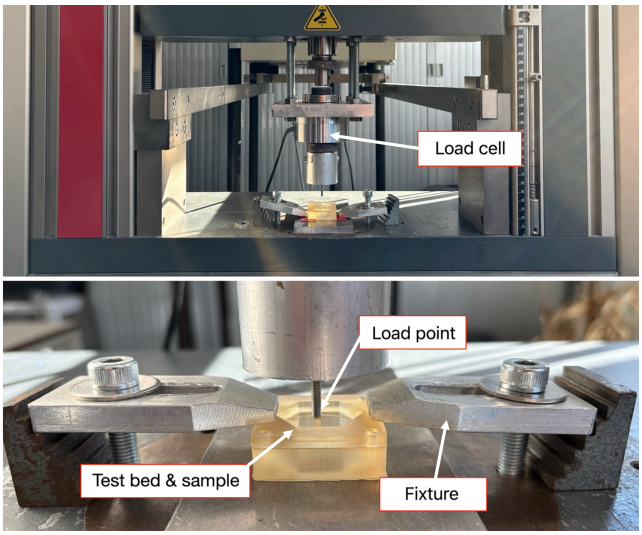

Fig. 2.8. Experimental test setup for a single unit cell using ZwickRoell Z005 uniaxial testing machine.

3.1. Fabrication

3.1.1. *Mould dimensional accuracy*

SLA printed moulds demonstrated good agreement with the designed models. Using the extremely small layer thickness of 0.025 mm, an acceptable feature size and surface finish was achieved. Figure B.2 shows individual layers of the mold features with geometric values. Even though layered steps are clearly defined in microscopic images, this had no effect on the surface finish of the formed unit cell due to high toughness of PEEK. Results tabulated in Table 3.1 compares height of the designed model against the printed sample. Generally, mould feature quality was well controlled demonstrating low deviation in height where each sample was maintained at >5 %. It was observed that moulds with cosine beam height of 3 mm and 4 mm demonstrated excellent feature quality by deviating just 1.43 % and 1.75 % from designed models respectively. Thus, it was assumed that all printed moulds in this reseach were geometrically acceptable for hot forming.

Table 3.1. Designed cosine beam feature height, h compared against SLA printed moulds.

Designed (mm)	Printed (mm)	Deviation (mm)
1.000	0.953	0.047
2.000	2.079	0.079
3.000	2.957	0.043
4.000	4.070	0.070

3.1.2. *Effects of hot-forming duration*

Total forming duration has significant effect on the geometrical accuracy of the unit cell. Below, in Figure 3.1, a F-d response dependency on the total forming time for the 100 µm thickness sheet is shown. It demonstrates

that the longer hot forming time directly affects the $F-d$ response shape and the force magnitude between the two equilibria. The results are presented in such way that the additional time (indicated by a '+' in the legend) is denoted as the cooling time, that is, when the moulds are no longer heated but stay compressed within the electric press. The expected shape of the response at the time of 360 s is poorly represented with F_{max} = 64 mN, whereas, F_{max} at ≥720 s produces well defined, consistent peak with maximum forces fluctuating between 94 mN and 107 mN. Therefore, the results indicate that forming a 100 µm PEEK substrate requires no less than 720 s for optimal performance. Similarly, this method was applied to 200 µm thick unit cells. It was observed that the optimal forming time must be at least 900 s to achieve the best results.

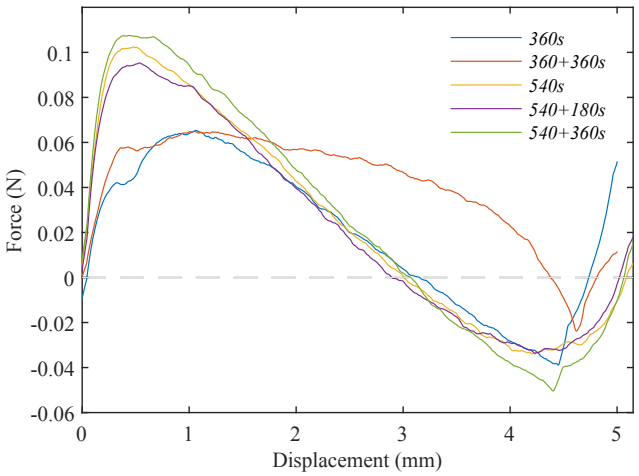

Fig. 3.1. Effects of forming time on the F-d response. Unit cell parameters: h = 3 mm, L = 10 mm, b = 2 mm at 100 µm thickness.

Furthermore, Figure 3.2 shows qualitative observations of the beam height, h dependency on the total forming time. The designed mould height was set at 3.0 mm. Evidently, it demonstrates that the effects of longer forming duration results in a more accurate geometrical form for the 200 µm thickness unit cell. The graph trendline illustrates that once the forming time had passed 1000 s, no further improvements were visible. Finally, the absence of material necking at the beam boundaries indicated stable material performance and geometric control.

3.1.3. Unit cell stress state

One of the more significant issues affecting feature quality in a hot forming process of solid polymers is the stress relaxation [15]. In this work, once hot formed, moulds were subjected to continuous 5 min compression in ambient temperature to mitigate any significant unit cell geometrical instabilities. However, more attention was needed to observe the effect of thermal residual stresses during the cooling process. In MEMS microfabrication, measurement of residual stress gradient in cantilevers is estimated via deflection of the beam and relative change of length along its axis [16]. Using this technique, a slender PEEK sample was hot formed. Qualitative test

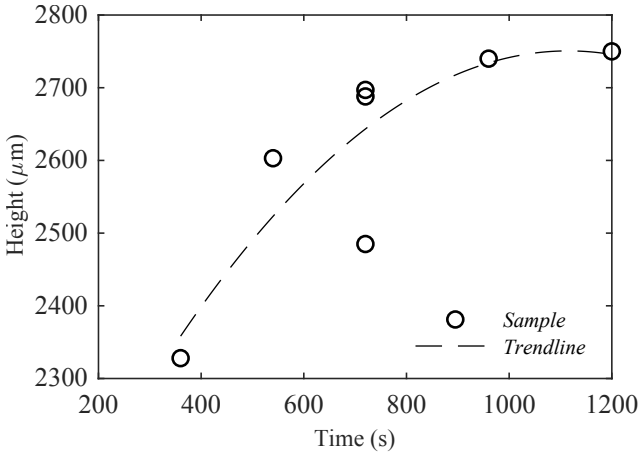

Fig. 3.2. Measured unit cell height versus the total hot forming time at 200 µm sheet thickness. Design parameters: h = 3 mm, L = 10 mm, b = 2 mm.

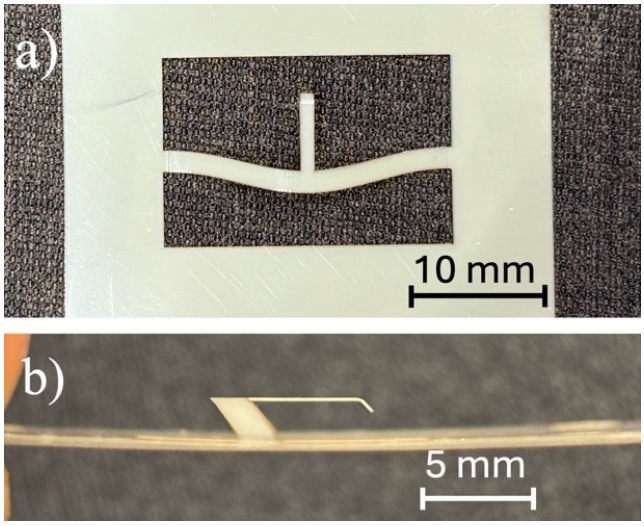

Fig. 3.3. Hot-formed PEEK sample for residual stress observation. Formed sample with cosine beam shape and a cantilever protrusion. a) Top view; b) Close up side view of the cantilever.

results revealed that no change in curvature or length of the slender beam was observed as shown in the Figure 3.3 suggesting that the fabrication technique used in this research is sufficient for geometrically stable features.

3.2. Single beam unit cell

3.2.1. Design

To confirm the MECOMOS fabrication method, single beam unit cell designs were investigated resulting in multiple variations of a single beam PEEK unit cell. Subsequently, this approach laid the foundation for further designs in this study. Initially, the most basic beam with standard parameters was chosen as shown in Table 3.2.

Table 3.2. Geometric parameters of the single beam unit cell.

l (mm)	h (mm)	t (mm)	b (mm)	Q	λ^{-1}
20.0	3.0	0.20	1.0	15.0	100.0

Based on prior conducted literature review shown in Appendix F, combination of such parameters was sufficient to achieve a Q factor well above 2.31 and $\lambda > 65$ and therefore, a bistable unit cell. The first design attempts demonstrated the feasibility of the fabrication method. However, it was established early in the study that the height dimensional error of the PEEK sample was within 5−10 % after hot forming. Although qualitative tests showed that the snap-through behaviour is present in the beam, it was not able to maintain a second equilibrium state. Furthermore, despite fabricating series of designs with varying beam dimensions, unit cells only showed diversity in snap-though transitions and not stable second equilibrium mode. Subsequently, it was concluded that the unit cell of homogeneous thickness cannot achieve bistability unless both, the correct geometrical relations and boundary conditions, are taken into account.

3.2.2. Local geometric tailoring

Another way for achieving bistability in a cosine beam is via boundary conditions: specifically, at the ends of the beam ($x = 0$ and $x = l$) or by restricting beam's second bending mode at the midspan of the beam. The latter was realised through locally increased surface area at the midsection as shown in Figure 3.4. Such modification resulted in increased second moment of area and bending stiffness, effectively replacing the necessity of a rigid pin to restrict the beam's second bending mode. Additional studies were conducted on the shape of the midspan section by adding stiffening features like boss and corrugations; however, numerical nor experimental tests confirmed any substantial improvements in the $F - d$ response. Another implemented improvement was local reduction of beam sections at the base. It was observed that a uniform thickness beam causes rotations at the boundary edges and therefore, by narrowing the sections, a flexure-like behaviour was enabled allowing easier snap-through deformation. Despite the effectiveness of these combined modifications, which were implemented in later designs of this study, they demonstrated inconsistent bistability for the single beam configuration.

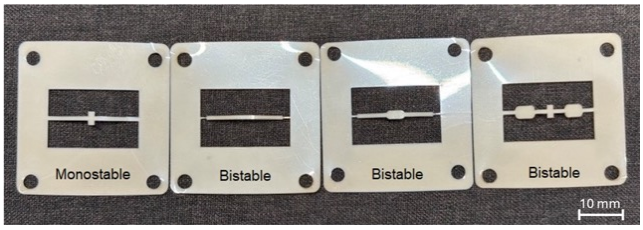

Fig. 3.4. Single cosine beam geometric modifications resulting in mono-, bistability.

To enhance sheet stiffness around the boundary conditions, geometry of the flat PEEK substrate was modified to optimise the bistable performance. In the automotive, construction, and aerospace sectors, bending sheet metal is a standard technique used to enhance the axial in-plane longitudinal and transverse stiffness of flat substrates [17]. By strategically modifying a part's geometry, specifically through the addition of local or global ribs, flanges, or corrugations, engineers can significantly improve load bearing capacity. Following this principle, corrugation of the flat surface around the cosine beam was investigated as illustrated in Figure 3.5. The trapezoidal and sinusoidal corrugations were applied throughout the sheet along the axis of the beam as shown in Figure 3.5 a) and b). In addition, corrugations were formed around the unit cell following the external edges of the open geometry, however, this did not improve bistable performance of the unit cell. In some cases, it was observed that corrugation patterns produced more flexible boundaries (due to direction of the pattern) or resulted in marginal bistability of the substrate around the unit cell. Despite experimental attempts, no substantial results were achieved however, more research is needed to draw definitive conclusions on effectiveness of hot-formed corrugations.

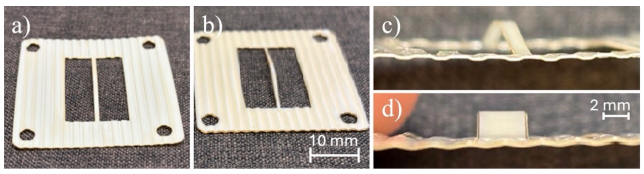

Fig. 3.5. Surface corrugation of the PEEK substrates: a) Trapezoidal corrugations for the single unit cell; b) Sinusoidal corrugations for the single unit cell; c) - d) Close up image of the profiles.

To conclude, even though a single beam unit cell design established the fabrication method using flat PEEK substrates, the actual bistable performance was dubious due to absence of necessary stiffness. All design modifications have only improved the smoothness of the snap-through transition with no effect to bistable performance. In addition, to fabricate a three-dimensional metastructure, more surface area for multilayer binding is needed which is insufficient for the 2D unit cell configuration explored in this work. Therefore, an alternative triple beam configuration was proposed.

3.3. Triple beam unit cell

Once the initial investigation into the single beam cell design was established, a more suitable unit cell structure was designed called the 'triple' unit cell. This geometric configuration was used to obtain the bulk of the results presented in this research.

3.3.1. Design

A triple beam configuration is shown in Figure 3.6 with its core geometric parameters. The general structure was derived from the previous work by Zhang et al. [3] in combination with the design language of a single unit cell where the half length, $l/2$ of the cosine beam was considered. For symmetry, a hexagonal cutout at the base was made where tree beams extend from each corner at 120 deg apart. In the middle, a circular platform was designed to restrict beam's second bending mode and provide substantial surface area to stack the individual layers. In Figure 3.6 b), a close up view depicts a narrow section which connects the cosine beam to

the base of the unit cell for flexure-like behaviour, at width $b/2$. Thus, combination of these features and significantly improved boundary conditions resulted in a functioning bistable 3D unit cell.

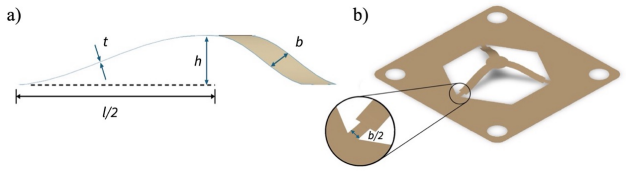

Fig. 3.6. Geometry of the 3D unit cell: a) Side profile; b) ISO view of the formed 3D unit cell.

The two primary unit cells with their corresponding geometries are summarised in the table below Table 3.3.

Table 3.3. Geometric parameters of the fabricated L10H3 and L6H2 unit cells.

	l (mm)	h (mm)	t (mm)	b (mm)
L10H3	10.0	3.0	0.20	2.0
L6H2	6.0	2.0	0.20	1.0

While the 3D cell structure in this research was formed using a minimum of three cosine beams, various higher order configurations have been explored in the literature by joining more beams at the center [18]. It was found that increased beam number leads to enhanced snap-through performance due to improved boundary conditions at the base achieving superior symmetric and smoother deformation. However, it simultaneously increases the peak force F_{max} and the overall mass of the unit cell. Although it was considered, to maintain design consistency and reduced complexity, this thesis focuses exclusively on a triple beam configuration.

3.3.2. Parametric study

Snap-through forces of the cosine beam are controlled via geometric architecture. Therefore, to better understand these effects, a parametric analysis was conducted. This includes varying the values of the three main variables t, h and b while remaining parameters were constant. The FEA numerical results were plotted and compared against the quasi-static experiments to gain a better understanding of the unit cell F-d response. However, as it will be observed from the graphs, the discrepancies in the distance magnitude between the FEA and experimental tests are attributed to the fabrication limits of the hot forming process.

The influence of height to F-d response is shown in Figure 3.7 comparing numerical and experimental data of the two PEEK unit cells at 100 µm and 200 µm thickness. As expected, both substrates exhibit a characteristic response across the variation of h. The decrease in beam's height results in monotonic reduction of peak positive force F_{max} and minimum force (F_{min}) while the overall qualitative shape of the curves remains invariant. This consistent scaling behaviour indicates well controlled and tunable scaling capacity if the unit cell. Although force magnitudes remained similar, a general shape of the experimental results indicate sharper snap-through transition compared to FEA. Discrepancies in displacement length across the 100 µm and 200 µm thickness unit cells are attributed to fabrication limits of the fabrication process.

The maximum experimental forces for the 200 µm thickness unit cell, shown in Figure 3.7 a), were $F_{max} = 0.918\,\text{N}$ and $F_{min} = -0.155\,\text{N}$ at $h = 4\,\text{mm}$. Contrary, peak positive and negative forces at $h = 1\,\text{mm}$ were $0.238\,\text{N}$ and $-0.025\,\text{N}$ respectively. Notably, extremely small F_{min} at $h = 1\,\text{mm}$ suggests that the beam is critically bistable where nominal amount of force would cause a snap-back into the first equilibrium. Although similar, the F-d response of the 100 µm unit cell showed sharper peaks at F_{max} as illustrated in Figure 3.7 b). This implies a less gradual transition between the stable states. In addition, it is observed that the F-d line at $h = 1\,\text{mm}$ and $h = 2\,\text{mm}$ aligns with the zero line, suggesting absence of a second equilibrium state. However, as noted from the qualitative tests, the second equilibrium is present and, therefore, such discrepancy can be attributed to the sensitivity limits of the measurement equipment. Likewise, the 50 µm thickness unit cell was characterised as shown in Figure B.9, where the quasi-static tests demonstrated general forces of two orders lower compared to the 200 µm thickness sample. As seen from the plot, the F_{max} at $h = 4\,\text{mm}$ was recorded as $0.015\,\text{N}$ and F_{min} as $0.009\,\text{N}$. Despite multiple attempts, test results at $h = 1\,\text{mm}$ and $h = 2\,\text{mm}$ failed to produce a characteristic profile of the bistable beam suggesting that the sensitivity of the 50 µm thick unit cell was beyond instrument's sensitivity limits. Generally, the F-d response for the 50 µm thick unit cell produced high fluctuations and erratic profile, making it difficult to quantify meaningful data and thus, it was excluded from the further analysis.

Parameter analysis of the effect of the beam width, b is depicted in Figure 3.8 a) which demonstrates less significant change in critical forces between the samples. Notably, tuning of the beam width may be the least significant parameter in designing a multi-stable mechanism. The widest cosine beam configuration, at $b = 2.5\,\text{mm}$, the F_{max} reaches $0.784\,\text{N}$ and F_{min} is $0.223\,\text{N}$ whereas at $b = 1.0\,\text{mm}$, the F_{min} demonstrates marginal stability only requiring $0.078\,\text{N}$ to transition to the first equilibrium state. Finally, the beam thickness has the biggest influence on the $F - d$ response of the unit cell. Results, tabulated in Table A.4 and shown in Figure 3.8 b) compare three unit cells of varying thickness at50 µm, 100 µm and 200 µm with dimensions $l = 10\,\text{mm}$, $h = 3\,\text{mm}$ and $b = 2\,\text{mm}$. Immediately, the most evident difference is observed in the maximum force magnitude. The 200 µm thickness unit cell shown in Figure 3.8 b), requires F_{max} of $0.685\,\text{N}$ which is almost a sevenfold difference in magnitude than the 100 µm unit cell at $0.102\,\text{N}$. Similarly, the 50 µm thickness substrate exhibits a magnitude lower critical force of $0.011\,\text{N}$. From the combined

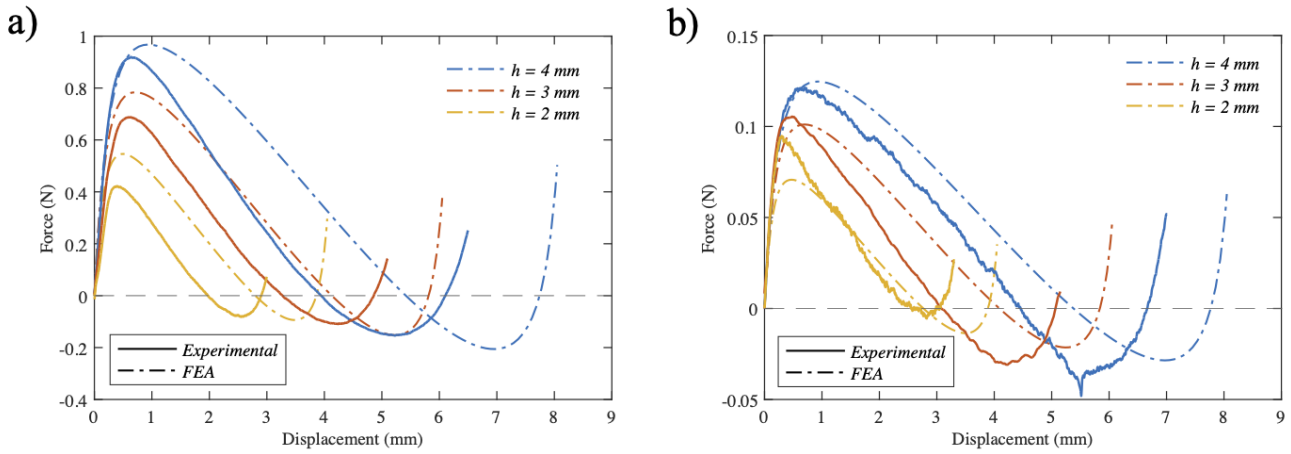

Fig. 3.7. Plotted F-d response of design parameter variation, h at $l = 10\,\text{mm}$ and $b = 2\,\text{mm}$: a) 200 µm sheet; b) 100 µm sheet.

unit cell thickness analysis it can be drawn that it is the most critical geometric parameter for controlling larger forces within the bistable structure. To conclude, the parameter study confirmed unit cell's highly tunable nature enabling substantial flexibility in tailoring the snap-through response. By combining these parameters, a hot-formed unit cell can achieve reliable bistable behavior and, in more complex configurations, predictable multi-stable performance.

3.3.3. Scalability

One of the advantages of bistable beams is its ability to comply with scalability. As long as boundary conditions provide enough stiffness, beam's behaviour is controlled via fine tuning of geometric parameters. Therefore, as long as parametric relationships are maintained, the size of the unit cell can be significantly reduced. To confirm this, scaled down samples, shown in Figure B.4, were fabricated and their dimensions tabulated in Table 3.4 where every sample was reduced in size by maintaining approximate $3:1$ length-to-height (l/h) ratio.

Table 3.4. Geometric parameters of fabricated triple unit cells. Investigating scalability limitations.

	l (mm)	h (mm)	t (mm)	b (mm)
L10H3	10.00	3.00	0.20	2.00
L6H2	6.00	2.00	0.20	1.00
L3H1	3.00	1.00	0.10	0.50
L1H05	1.00	0.50	0.10	0.25

It was observed that each reduced sample maintained their second equilibrium mode without a snap-back, confirming the design space at any desired scale as long as the fabrication method is viable. On the other hand, to confirm hot forming limits, a L1H05 sample was fabricated using the 100 µm substrate with feature size of 500 µm. However, microscopic images taken at x50 zoom ratio revealed significant geometric imperfections (shown in Figure B.5). The cosine beam profile was extremely distorted with central connection point tilted away from the vertical axis, effectively losing the symmetry required for the snap-through deformation. Furthermore, difficulties of displacing the unit cell into the second equilibrium state were present and no quasi-static tests were conducted due to resolution limits of the measurement equipment. Consequently, geometric flaws observed in the L1H05 unit cell can be attributed to multiple factors: insufficient resolution of the mold, variations within the hot forming process and the requirement of using substrates measuring $\leq$100 µm in thickness. This is consistent with prior research establishing that feature accuracy degrades significantly below 400 µm. Therefore, this study only focuses on the development of the L10H3 and L6H2 unit cells.

3.3.4. Multi-cell lattice

Following the single cell analysis, the design was scaled to a multi-cell architecture integrated onto a PEEK substrate. Given the limitations of the experimental setup, a L6H2 unit cell geometry was adopted to fit three distinct unit cells on a single sheet to form a 3×1 structure. The specific dimensions of the L6H2 configuration are tabulated in 3.4. As shown in Figure 3.9 a), to optimise lattice footprint within the 35 mm × 35 mm area, unit cells were arranged in a honeycomb structure, while maintaining a 1.73 mm gap inbetween. Advantage of such honeycomb arrangement is the in-plane symmetry of the structure which enables multi-axes tilting or rotational DoF (degrees of freedom) in multilayered systems as per previous study [3]. Some experiments were conducted with two adjacent L6H2 unit cells, however, a single in-plane symmetry did not demonstrate any stable tilting configuration. Furthermore, as shown in Figure 3.9 a), 0.5 mm tall extruded features were added on a 3×1 lattice. Such feature carries a twofold functionality - to provide an additional step precision and to reduce a contact surface area between the collapsing layers. The presence of a 1 mm gap between each layer enables greater control over the step size of the displaced row. However, the height of the extrusion is crucial, as it was observed that a 0.75 mm tall feature reduced the clearance required for snap-through deformation, rendering the unit cell monostable.

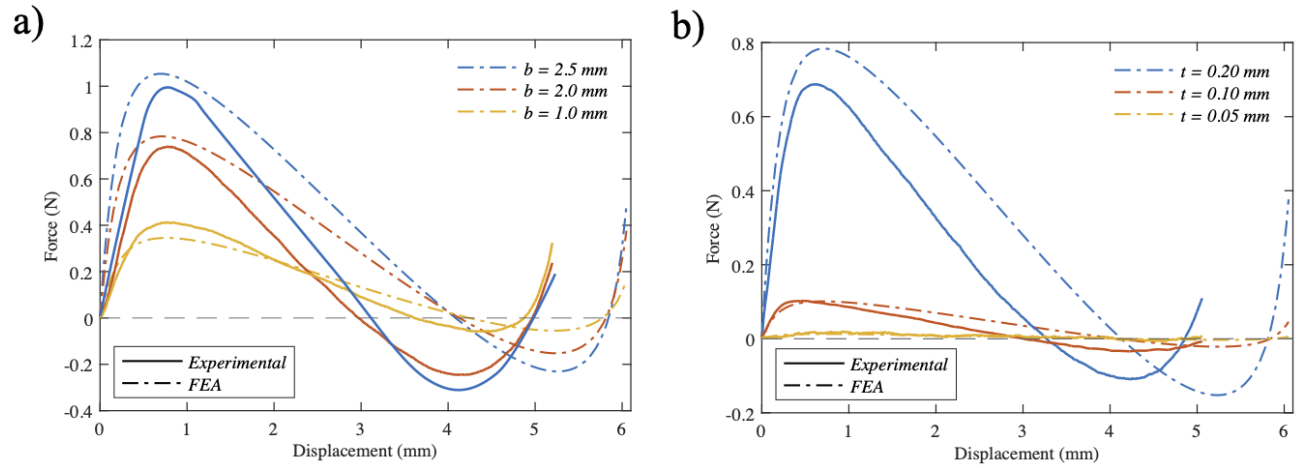

Fig. 3.8. Plotted F-d response of design parameter variations at $l = 10\,\text{mm}$ and $h = 3\,\text{mm}$: a) Variation of beam width at $t = 200\,\mu\text{m}$; b) Variation of beam thickness at $b = 2\,\text{mm}$.

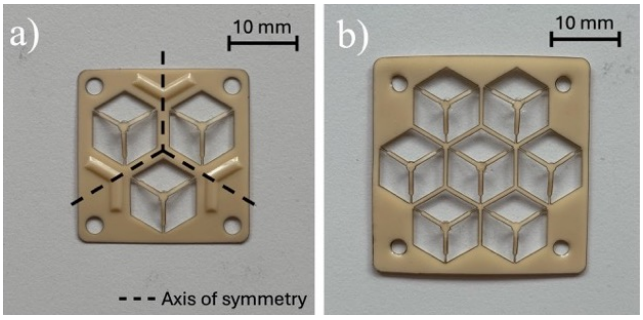

Fig. 3.9. The L6H2 multi-cell lattice: a) 3×1 arrangement; b) 7×1 arrangement.

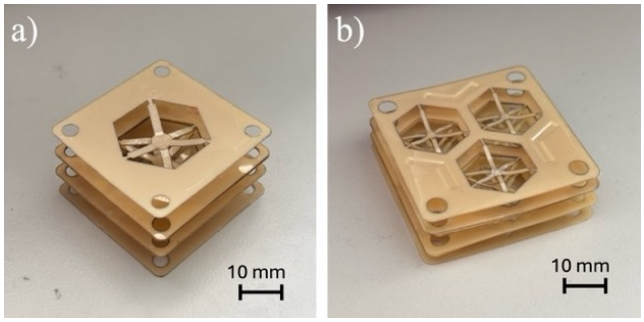

Fig. 3.10. 3D multi-stable metamaterial: a) 1×4 structure using L10H3 unit cells; b) 3×4 structure using L6H2 unit cells.

To explore larger number of in-plane symmetric axis, further lattice design implemented a higher order of unit cells (from 3 to 7) on a $40 \times 40\,\text{mm}$ substrate while maintaining other geometric parameters. The resulting multi-cell layer 7×1 is displayed in Figure 3.9 b). Although individual unit cells demonstrated bistability, this negatively affected the total stiffness of the sheet where resulting PEEK layer exhibited flexible perforated surface-like behaviour. Therefore, it was assumed that the multilayered structure combined from such layers would result in an unpredictable response leading to poor multistability performance. Hence, the seven cell lattice design was not investigated further.

3.3.5. *Multilayered structure*

By utilising the gained knowledge into single unit cell behaviour and lattice arrangement of multiple unit cells on a layer, a combined multi-stable structure was designed as show in Figure 3.10. Figure 3.10 a) shows a 1×4 arrangement containing four row layers assembled by stacking and bonding six L10H3 200 µm unit cells together. Similarly, Figure 3.10 b) displays 3×4 metastructure containing six L6H2 stacked multi-cell sheets assembled together by combining 100 µm and 200 µm thick substrates. A more detailed layer assembly sequence is shown in Figure B.7. To prove the concept, only three rows were stacked; however, there is no limit to the maximum number of layers.

3.3.6. *Deterministic deformation*

In this work, a deterministic deformation sequence was achieved through thickness variation. Deformation of the 1×4 metastructure is depicted in Figure 3.11 a). It shows a row collapse sequence of $1 \rightarrow 2 \rightarrow 3$. Figure 3.11 b) demonstrates row deformation sequence for the 3×4 metastructure in a $3 \rightarrow 2 \rightarrow 1$ order. It was observed that the deformation sequence of the 1×4 metastructure is random due to identical thickness of unit cell layers where other samples demonstrated deformation sequence of rows $1 \rightarrow 3 \rightarrow 2$, indicating that current assembly method is viable for any desired configuration. Referring to the layer stacking, discussed in section 2, row collapse sequence is influenced by arrangement of varying thickness layers. To achieve the sequence shown in Figure B.7, the stiffest layer (row 1) bonded two 1×3 200 µm sheets together. The second row (row 2), bonded two 1×3 layers 200 µm and 100 µm thick. Lastly, just as with the base layer, the top layer is a single 1×3 100 µm lattice.

The following graphs shown in Figure 3.12 present a F-d response of the multilayer mechanisms and compares the FEA against the experimental results. Figure 3.12 a) displays snap-through deformation response of the 1×4 structure relating three critical force peaks (F_{max})

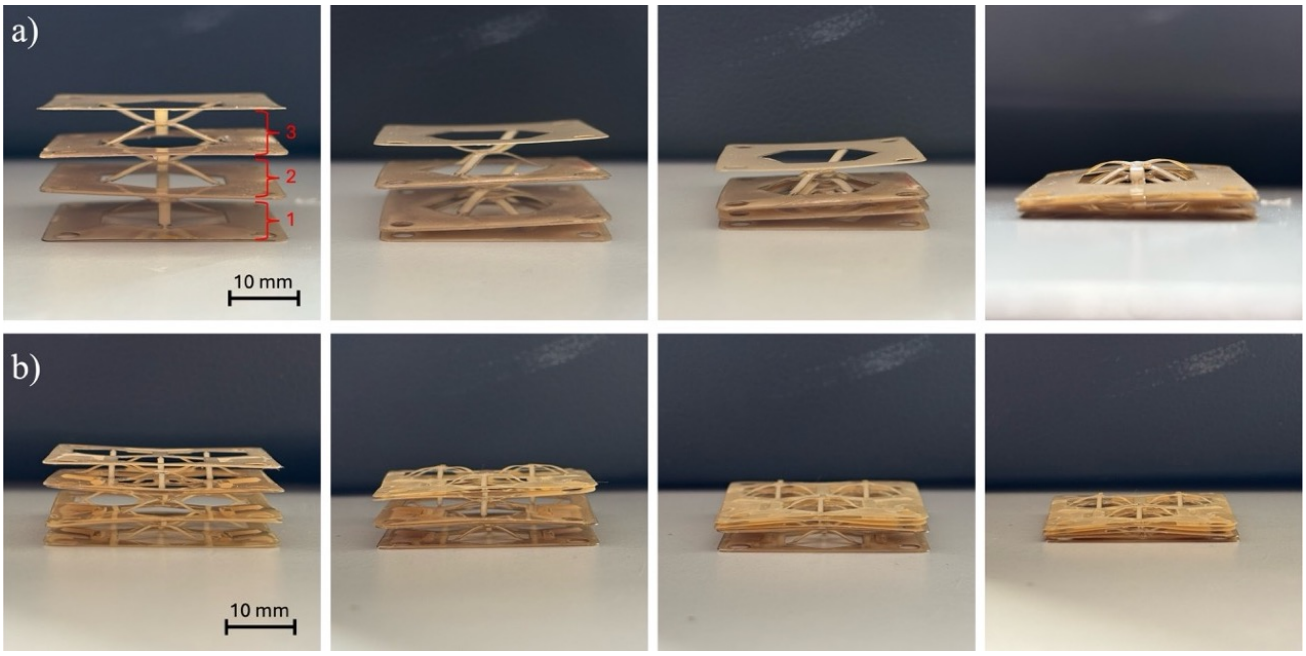

Fig. 3.11. Deterministic collapse sequence of multi-stable metamaterial: a) Rows $1 \rightarrow 2 \rightarrow 3$ for the 1×4 metastructure; b) Rows $3 \rightarrow 2 \rightarrow 1$ for the 3×4 metastructure.

to the collapsing row number. Generally, the FEA and experimental results are in good agreement by capturing the irregular shape of the peaks due to inherent structure of the metamaterial. Such phenomena is attributed to the small connection point at the apex between the adjacent unit cells which is caused by the pivot-like deformation. This leads to the rotational freedom of the middle layers during the quasi-static deformation as shown in Figure B.8 b). Here, instead of instantaneous deformation of all beams, a partial deformation in the unit cell causes 'double' peaks with the magnitude $F_{max} = 0.61\,\text{N}$. Just as in the FEA, experimental work confirmed the presence of the third critical force peak. Since the stiffness of the multi-stable metamaterial boundaries is not ideal, the third maximum peak indicates a combined force from the previous two layers and thus, requires three times the force to collapse the final row at $F_{max} = 1.65\,\text{N}$.

The $F-d$ response of a 3×4 mechanism, assembled from three L10H3 unit cell lattices, is shown in Figure 3.12 b). Similarly to the 1×4 structure, three maximum force peaks are present confirming the total row number. In this case, however, individual rows exhibit only the translational deformation where rotations during the quasi-static test were well controlled. Consequently, all the F_{max} peaks exhibit well defined curved shape with no non-jagged slopes. This is attributed to increased number of connection points at the each layer creating an in-plane three point support for each row. Contrary to the 1×4 system, discrepancies in FEA and experimental results are substantially more evident due to much more complex topology of the lattice. The most significant difference is in the shape and the magnitude of the force response. The FEA estimates that the first and the second row require approximately 0.5 N of force to snap, whereas quasi-static experiment revealed that it requires 0.2 N and 0.6 N respectively. Moreover, the experimental force magnitude of the third peak, F_{3max}, greatly undervalues the FEA data by as much as two times and is equal to 1.41 N. Although different sheet thicknesses were used in the fabrication of the 3×4 metastructure, based on the discrepancies seen in the $F - d$ graph, it is unclear how it affects quantitative response of the multi-stable system. Finally, numerical results indicate the absence of multi-stability (does not cross the zero line), nonetheless, experimental data reveals otherwise. Therefore, it can be concluded, that modeling of the thin sheet bistable geometries requires much more time beyond the scope of this work.

3.3.7. Rotational compliance

As mentioned in the previous section, a 3×1 multi-cell lattice was designed so that the combined mechanism exhibits a tilting stability as depicted in Figure 3.13. However, it was observed that the biased stability of the tilted state occurs only between the middle layers and cannot be sustained at all three axis of symmetry. That is, the tilting is only observed on one side as shown in Figure 3.13. This discrepancy is attributed to two conditions: instabilities within the partial deformation of individual beams and the amount of PEEK substrate around the individual cell. Therefore, referring to Figure 3.9 a), only the bottom unit cell satisfies these conditions and subsequently, exhibits biased tilting. As illustrated in Figure 3.13, the absence of rotational compliance of the top and bottom layers is attributed to inadequate structural stiffness. To confirm this assumption, some experimental observations were conducted by bonding a 3 mm thick SLA printed plate with the top layer. The results confirmed that once the plate was attached to the multi-stable structure, the top layer exhibited tilting, enabling additional degree of rotation. Therefore, it is evident that all multi-structure rows per-

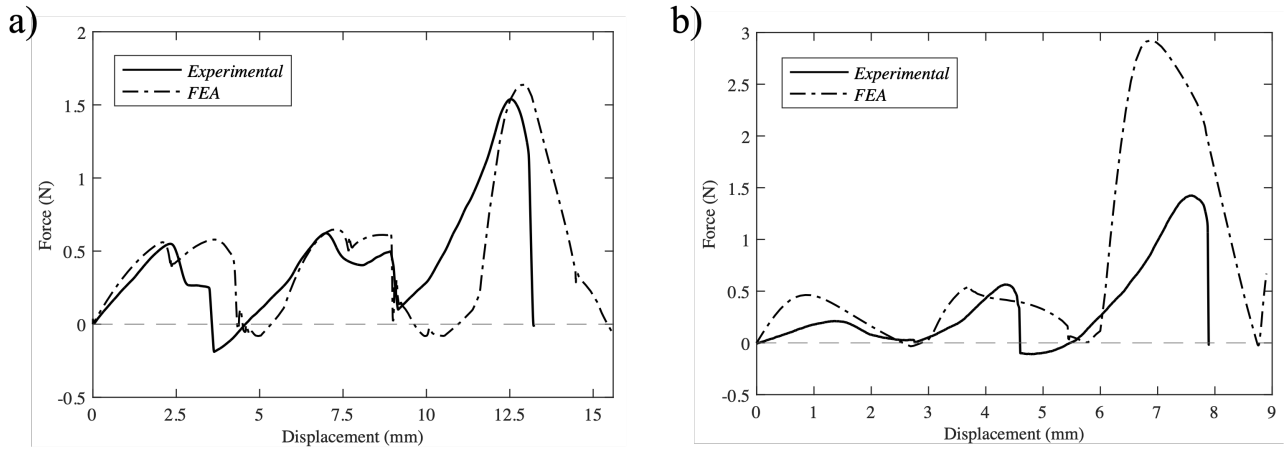

Fig. 3.12. Plotted F-d response of the multi-stable mechanism: a) 1×4 structure; b) 3×4 structure.

mit controlled angular rotation once sufficient stiffness is present within the multi-cell layers.

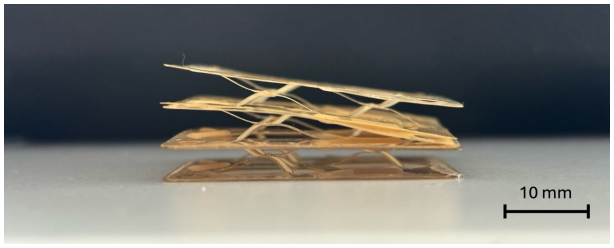

Fig. 3.13. Tilted stable configuration of the 3×4 metastructure.

3.4. Process limitations

The experimental phase of the thesis revealed multiple challenges in the MECOMOS fabrication process which includes mould quality, bonding and assembly of the metastructure. Each stage had their own unique set of difficulties affecting the quality of the final multi-stable metastructure. Firstly, the mould quality must be addressed. Just as with every replication-based fabrication method, it is imperative to have parallel moulds. In the initial stages of the research, moulds exhibited unusually high number of cracking after being used fewer than 3 to 4 times. Cracks typically originated around the feature edges or between the two adjacent surfaces indicating a localised stress concentration. Although these defects did not visibly compromise the geometry of the formed unit cell, it was expected that a high cracking frequency may negatively impact process repeatability. Subsequently, further investigation revealed that the flexible base used for mould printing (for easier removal) was insufficient for printing parallel surfaces and therefore, negatively impacted pressure distribution during the hot forming. Although it was only observed twice, a non-parallel alignment resulted in localised fusion of the moulds at the open geometry of the PEEK unit cell, as illustrated in Figure B.6. Nonetheless, the final moulds used in this study were printed on an alternative support base resulting in a stable performance and deliverables.

Due to nature of the PEEK substrate, it is difficult to achieve rigid bond between the unit cells. Although effectiveness of the cyanoacrylate was sufficient for all designs and assembly of the cell layers in this work, the solution is not reliable for long-term use nor for multi-cell lattice bonding due to brittleness of adhesives. Unique feature of the triple beam unit cell is the center platform, a flat section designed for connecting unit cells, however, the surface area is significantly reduced once the size of the unit cell is scaled down and therefore, substantially increasing complexity of adhesive application. These issues were extremely evident in bonding of the 7×1 lattice where multiple attempts were made to accurately match the surfaces during the short cyanoacrylate solidification window. Besides layer bonding, cyanoacrylate was utilised to adhere multi-stable structure to the test bed for experimental validation. This resulted in extensive use of the adhesive compound since achieving a substantial bond between PEEK and the cured print resin proved difficult, causing experimental failure. Finally, whilst cyanoacrylate provided enough stiffness to prototype and conduct tests, lack of elasticity in bond strength of the glue showed degradation over multiple snap-through deformation cycles causing slight delamination between the layers.

This research showed that the snap-through deformation of a multi-stable metastructure exhibits high tolerance towards the assembly process and cell alignment. Despite joining the cell lattice as described in section 2, manual assembly is suboptimal for small scale structures. In precision engineering, special pins or geometries are used to precisely align structural components together resulting in accurate positioning, leaving tiny margins for error. Nonetheless, this technique was not applied in this research. Early attempts included using a bespoke assembly setup where unit cell lattice were aligned by using four rods inserted into corner apertures. Despite these efforts, such arrangement did not eliminate slight rotations along the x and y axis due to flatness imperfections at the centers of the triple unit cell. Therefore, after observing no improvements in assembly quality, manual assembly was implemented for multi-stable structures due to procedural simplicity and time efficiency.

4. CONCLUSIONS AND FUTURE WORK

4.1. Conclusions

Inspired by the previous studies, this work demonstrated a combination of fabrication processes to design a novel small-scale multi-stable metamaterial by utilising the hot forming of thin PEEK substrates. The overall findings of this research are divided into two sections: by presenting contributions to the MECOMOS project and the design of multi-stable mechanical metamaterials.

Following the MECOMOS methodology, it was confirmed that a functioning, millimeter scale bistable unit cell can be formed using the replication-based fabrication process. Building upon the previously existing approach, the laser cutting and hot-forming parameters were optimised. Experimental work demonstrated critical influence of the forming duration on the dimensional stability of the unit cell. It showed that more than 720 s and 900 s are required to form 100 µm and 200 µm PEEK substrates respectively. Furthermore, contrary to prior findings, observations indicated that the samples must undergo ambient cooling for 4−5 min prior to demoulding. Finally, qualitative tests confirmed the absence of internal residual stresses in the hot-formed cosine beams confirming the dimensional stability of the milimeter-scale features.

The majority of the results of this thesis are associated with the design of the unit cell and the multi-stable metastructure. Early investigations were conducted to confirm the viability of the MECOMOS method for designing a bistable unit cell. Experiments revealed that when utilising a substrate of homogeneous thickness, simply following basic dimensional relationships as the Q factor, λ ratio or h/l ratio is insufficient. Instead, additional stiffness around the boundaries must be integrated to avoid undesired axial rotations during the snap-through deformation. To mitigate this behaviour, local modifications like midspan section enlargement, a reduction of the beam width at the edges and the corrugation of the flat base were implemented. However, due to subpar bistability and the absence of stacking capabilities, an improved 3D unit cell lattice was created. The implementation of a three cosine beam design demonstrated multiple advantages in this work. It identified the unit cell fabrication limits, enhanced stiffness at the boundary due to geometric symmetry, enabled multi-cell lattice design and permitted assembly of a multi-stable system. A parametric study confirmed high sensitivity to geometric variations with peak forces ranging below 1 N, however, discrepancies in absolute displacement between the experimental and FEA models indicated geometrical deviations due to the fabrication methods. A study of the scaled-down samples revealed the minimum feature size of the cosine beam to be 500 µm which conforms with prior studies. Further designs demonstrated multi-cell capacity by fitting up to seven unit cells on a single substrate, however, this resulted in significantly reduced stiffness and poor lattice bistability. On the other hand, a three cell lattice (3×1) exhibited well defined snap-through deformation which was subsequently integrated into a multi-stable metastructure. The snap-through performance of the multi-stable metamaterial was evaluated through deterministic row deformation via thickness variation of the lattice layers, demonstrating that the assembly sequence of the PEEK layers is critical. Besides deterministic deformation, a three cell lattice multi-stable metamaterial (3×4) demonstrated rotational degree of freedom due to multiple axis of symmetry enabling higher order functionality compared to conventional multistable mechanical mechanisms.

4.2. Future work

The results of this work showed that a functioning multi-stable mechanism can be designed, fabricated and characterised. Nonetheless, the mechanical structure is a proof-of-concept and therefore, provides a foundation for further improvements. The future work can be split into three directions: refining the fabrication process to improve consistency, optimise geometric architecture of the unit cell and enhance the assembly method for improved stability and performance.

Fabrication process improvements:

- Hot forming: Investigate hot forming parameters beyond the $T_g = 150$℃ of PEEK. This way, the 100 µm and 200 µm thick substrates should exhibit more compliancy, potentially reducing the forming time and improving the shape accuracy.
- Multimaterial: Incorporate a multimaterial approach for stiffening the boundary conditions. A PEEK substrate can be sandwiched between the two PMMA sheets at $T_g = 150$℃ resulting in a thermally bonded layer and significantly improved thickness around the area of the unit cell. This way, no geometric manipulations would be needed to achieve the desired stiffness.

Optimisation of a geometric structure:

- Beam shape: Explore various beam shapes and their effects for the snap-through response on the unit cell leading to a more pronounced bistability and mechanical response.
- Cell shape: Design a 3D unit cell beyond the three beams. Even adding an additional cosine beam would create a perfectly symmetrical two axis design, potentially improving the rotational compliance and stability. In addition, analyse the rotational stiffness, to capture rotational deformation of adjacent cell elements.
- Boundary conditions: More in-depth research is required to assess the stiffness effects around the individual unit cells in a multi-cell lattice. This way, multiple cells can be designed on a single substrate allowing finer snap-through control and enable localised bistability within the structure.
- Assembly: Create a DFA (design for assembly) compatible unit cell lattice to improve stacking.

This includes hot forming small pins into the center portion of the 3D unit cell, enabling direct mating of the two layers and resulting in a more precise assembly.

Assembly enhancements:

- Setup: An improved assembly setup is required to restrict all rotational DOFs (degrees of freedom) during the assembly process to ensure a perfect alignment of multiple unit cells.
- Bonding: A better bonding method is needed. Research potential cyanoacrylate alternatives with more efficient application methods for bonding multiple unit cells. This way, a more rigid and delamination resistant structure can be designed.

References

[1] J. Sun and J. Zhou, "Metamaterials: The Art in Materials Science", *Engineering*, vol. 44, pp. 145–161, 2025.

[2] X. Tan, B. Cao, X. Liu, *et al.*, "Negative stiffness mechanical metamaterials: A review", *Smart Materials and Structures*, vol. 34, 2025.

[3] Y. Zhang, Q. Wang, M. Tichem, and F. Van Keulen, "Design and characterization of multistable mechanical metastructures with level and tilted stable configurations", en, *Extreme Mechanics Letters*, vol. 34, p. 100 593, 2020.

[4] H. Yang and L. Ma, "1D and 2D snapping mechanical metamaterials with cylindrical topology", *International Journal of Solids and Structures*, vol. 204-205, pp. 220–232, 2020.

[5] C. S. Ha, R. S. Lakes, and M. E. Plesha, "Design, fabrication, and analysis of lattice exhibiting energy absorption via snap-through behavior", *Materials & Design*, vol. 141, pp. 426–437, 2018.

[6] F. Tobias, F. Claudio, K. Muamer, G. Peter, and W. Martin, "Tailored Buckling Microlattices as Reusable Light-Weight Shock Absorbers", *Advanced Materials*, vol. 28, no. 28, pp. 5865–5870, 2016.

[7] J. Herder *et al.*, *Mechanical metamaterials for compact motion systems (mecomos)*, TU Delft, Ed.

[8] M. Rings, "Microscale hot forming of PEEK", MSc thesis, Technische Universiteit Delft, 2024.

[9] J. Qiu, J. Lang, and A. Slocum, "A Curved-Beam Bistable Mechanism", en, *Journal of Microelectromechanical Systems*, vol. 13, no. 2, pp. 137–146, 2004.

[10] X. Ju, S. Li, Y. Zhang, P. Wu, and Y. Li, "Design of multi-stable metamaterial cell with improved and programmable energy trapping ability based on frame reinforced curved beams", *Thin-Walled Structures*, vol. 202, p. 112 120, 2024.

[11] Y. Zhang, M. Tichem, and F. van Keulen, "Concept and design of a metastructure-based multistable surface", *Extreme Mechanics Letters*, vol. 51, 2022.

[12] K. Che, C. Yuan, J. Wu, H. Jerry Qi, and J. Meaud, "Three-Dimensional-Printed Multistable Mechanical Metamaterials With a Deterministic Deformation Sequence", *Journal of Applied Mechanics*, vol. 84, no. 1, 2017.

[13] D. P. Jones, D. C. Leach, and D. R. Moore, "Mechanical properties of poly(ether-ether-ketone) for engineering applications", *Polymer*, vol. 26, no. 9, pp. 1385–1393, 1985.

[14] M. A. Islam, M. H. Mobarak, M. I. H. Rimon, *et al.*, "Additive manufacturing in polymer research: Advances, synthesis, and applications", *Polymer Testing*, vol. 132, p. 108 364, 2024.

[15] J. Wang, P. Yi, Y. Deng, L. Peng, X. Lai, and J. Ni, "Recovery behavior of thermoplastic polymers in micro hot embossing process", *Journal of Materials Processing Technology*, vol. 243, pp. 205–216, 2017.

[16] T.-J. Peters and M. Tichem, "Fabrication and characterization of suspended beam structures for SiO_2 photonic MEMS", *Journal of Micromechanics and Microengineering*, vol. 25, no. 10, 2015.

[17] T. Yokozeki, S.-i. Takeda, T. Ogasawara, and T. Ishikawa, "Mechanical properties of corrugated composites for candidate materials of flexible wing structures", *Composites Part A: Applied Science and Manufacturing*, vol. 37, no. 10, pp. 1578–1586, 2006.

[18] Y. Dong, T. Yu, and Z. Zhang, "Design and mechanical analysis of 3D negative-stiffness curved domes with Bessel-functional profile", *Composite Structures*, vol. 304, p. 116 422, 2023.

A. Tables

A.1. FEA mesh study parameters

Table A.1. FEA mesh study parameters. As part of the numerical model, the acceptable miminum element size was evaluated. Models were run at different global element sizes for the beam size $l = 10\,\text{mm}$, $h = 3\,\text{mm}$, $b = 2\,\text{mm}$. Balancing runtime and model accuracy, a = 0.50 mm was selected as optimal element size.

Element size (mm)	Runtime (s)	Element no.	F_{max} (N)	Error (%)	$-F_{max}$ (N)	Error (%)
a = 2.00	28	74	0.8745	7.84	0.5546	12.42
a = 1.00	34	135	0.8421	3.78	0.5169	4.78
a = 0.50	40	306	0.8267	1.89	0.5106	3.45
a = 0.25	75	1110	0.8209	1.17	0.5054	2.45
a = 0.10	430	7610	0.8114	-	0.4933	-

A.2. Effects of hot forming duration

Table A.2. Unit cell hot-forming duration influence on formed height, h. Designed triple unit cell dimensions are $l = 10\,\text{mm}$, $h = 3\,\text{mm}$ at 100 µm thickness. Table results indicate that optimal total forming time for 100 µm PEEK substrate is 720 s.

Press time (s)	Cooling time (s)	Total time (s)	Height, h (µm)	Error %
360	-	360	2328	22.4
360	360	720	2485	17.2
540	-	540	2603	13.3
540	180	720	2697	10.1
540	360	900	2740	8.7
720	-	720	2688	10.4
1200	-	1200	2736	8.8

A.3. OPTEC laser parameters

Table A.3. OPTEC laser system parameters for processing PEEK laser substrates.

Parameters	50 (µm)	100 (µm)	200 (µm)
Diode current (A)	-	4	5
Mark speed (mm/s)	150	150	150
Jump speed (mm/s)	200	200	200
Laser fire rate (kHz)	50	50	50
Burst time (ps)	1000	1000	1000
Repetitions	15	15	20

A.4. Substrate thickness influence on maximum and minimum force

Table A.4. Comparison between FEA and experimental results of F_{max} and F_{min} at varying substrate thickness. Triple beam unit cell (L10H3) with dimensions of $l = 10\,\text{mm}$, $h = 3\,\text{mm}$, $b = 2\,\text{mm}$ (refer to Figure 3.7).

Thickness (µm)	Num. F_{max} (N)	Exp. F_{max} (N)	Diff (%)	Num. F_{min} (N)	Exp. F_{min} (N)	Diff (%)
$t_1 = 200$	0.784	0.687	13.18	−0.109	−0.152	32.95
$t_2 = 100$	0.102	0.101	0.99	−0.034	−0.021	47.27
$t_3 = 50$	0.018	0.013	32.26	−0.006	−0.003	66.67

B. Figures

B.1. Mould general dimensions

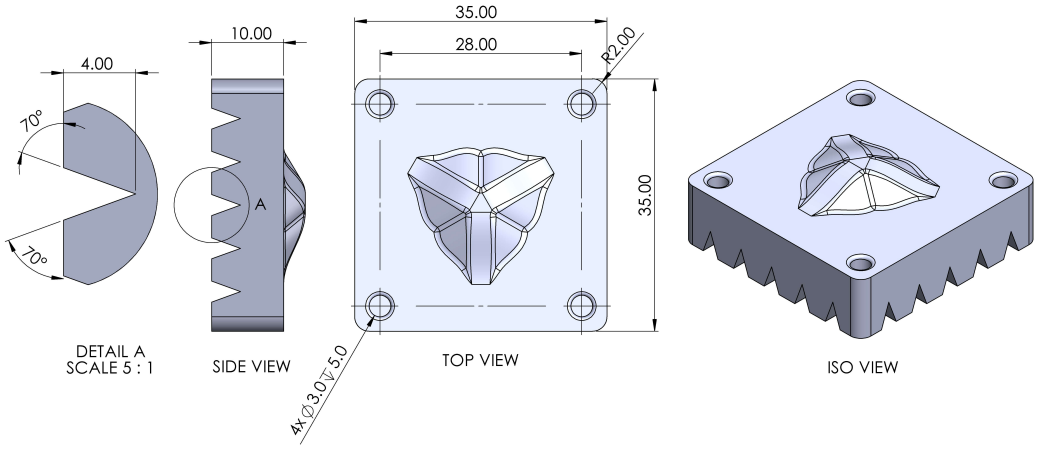

(a) Positive mold - L10H6.

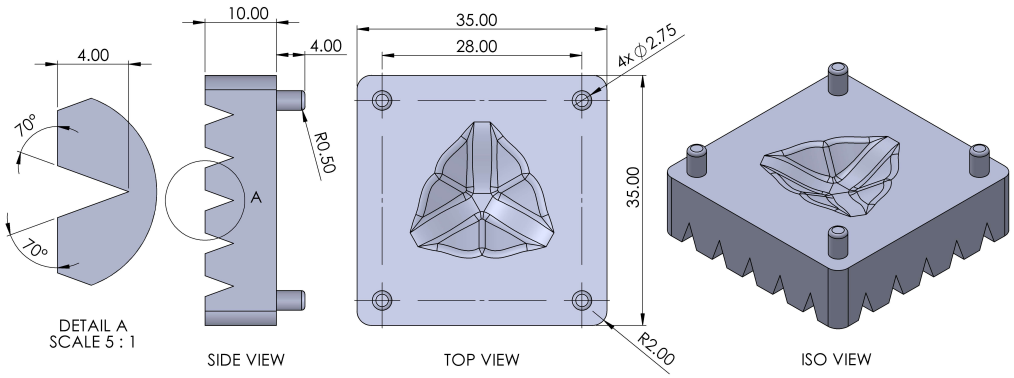

(b) Negative mold - L10H6.

Fig. B.1. General dimensions of the positive mold and negative moulds.

B.2. Mould surface and geometry

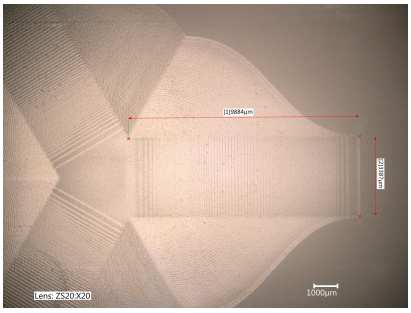

(a) Sample 1: L10H3 positive mould.

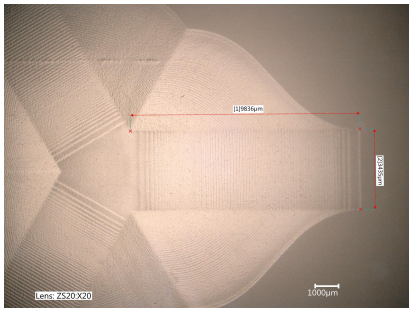

(b) Sample 2: L10H3 positive mould.

Fig. B.2. Microscopic image of the mould at x20 zoom.

B.3. Unit cell test bed assy

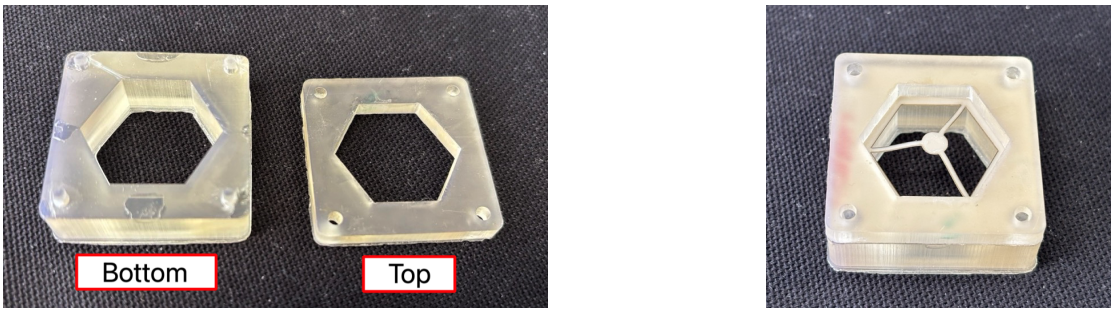

(a) Test bed assembly, Top and bottom parts.

(b) Assembled unit cell testing structure.

Fig. B.3. Test assembly: a) Test bed assembly for a single unit cell; b) Test bed assembly for multi-stable metastructure.

B.4. Scaled unit cells

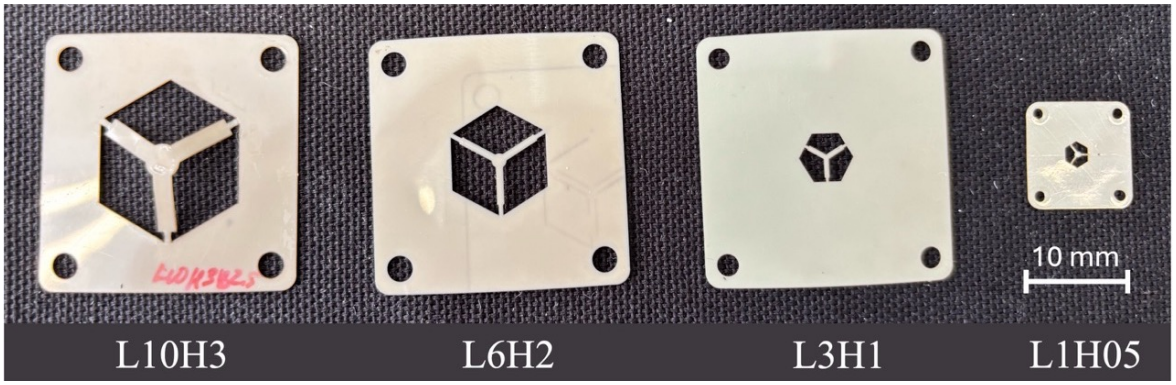

Fig. B.4. Triple cosine beam designs scaled from l =10 mm to l =1 mm.

B.5. L1H05 Unit cell

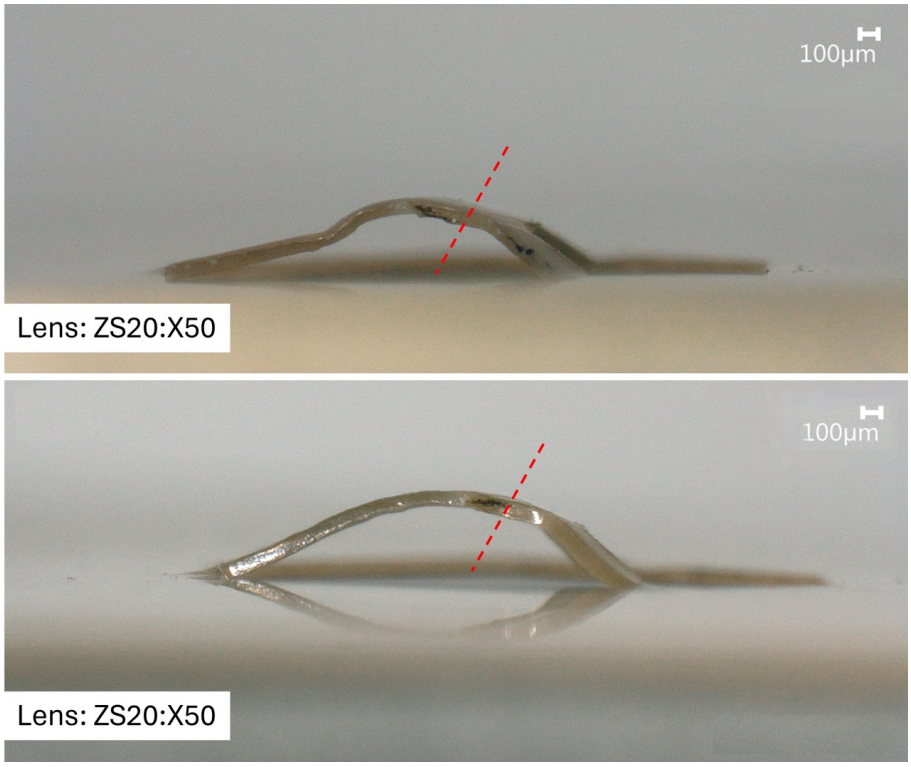

Fig. B.5. Side view of a triple beam PEEK unit cell (L1H05) with dimensions $l = 1$ mm, $h = 0.5$ mm, $b = 0.5$ mm.

B.6. Thermally fused moulds

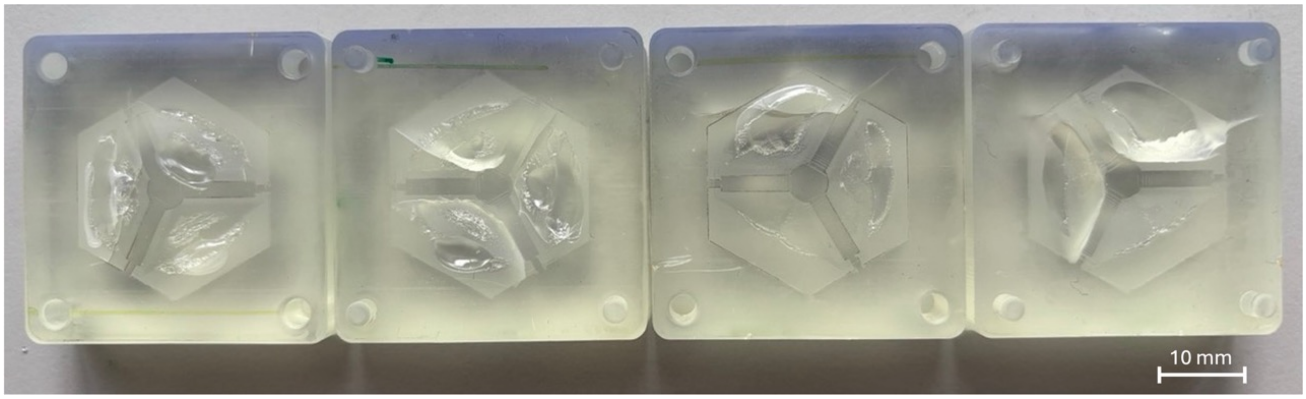

Fig. B.6. Samples of thermally fused moulds for the triple beam unit cells. Due to insufficient parallelism between the moulds, certain pressure/contact points started melting.

B.7. Assembly arrangement

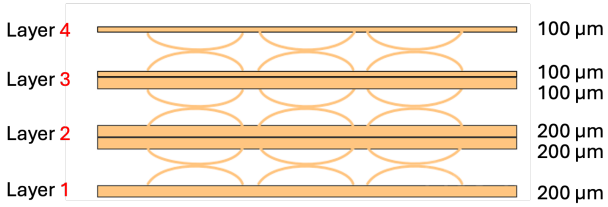

Fig. B.7. Assembly layer arrangement for the L6H2 3×4 multi-stable mechanism.

B.8. Multi-stable system test setup

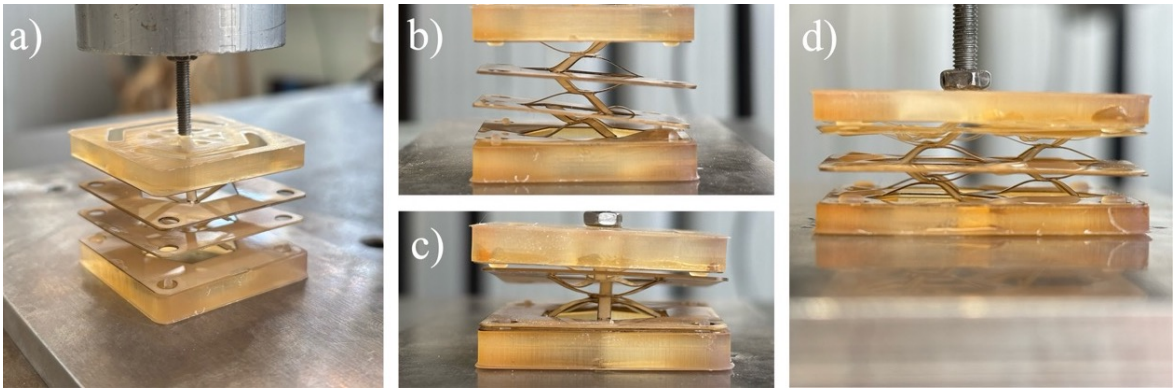

Fig. B.8. Experimental test setup for a multi-stable metastructure using ZwickRoell Z005 uniaxial testing machine. Similarly, to the single unit cell setup, bespoke top and bottom parts were printed and adhesively bonded to support the structure: a) 1×4 mechanism; b) & c) Tilted layer deflection during the quasi-static test of 1×4 mechanism; d) 3×4 mechanism.

B.9. Plotted *F-d* response at 50µm thickness

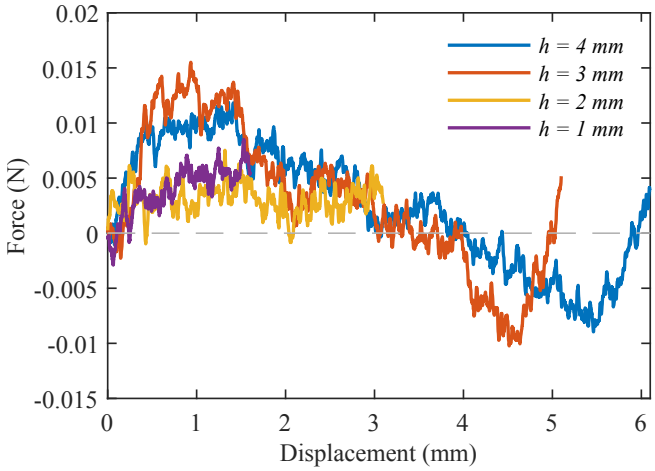

Fig. B.9. Recorded F-d response for triple beam 50 µm thickness unit cell. Plotted results of changing h at $l = 10\,\text{mm}$, $b = 2\,\text{mm}$.

C. Metamaterial fabrication process

D. PEEK sheets APTIV FILMS 1000

APTIV™ FILMS 1000

General Information

Product Description

APTIV 1000 series films are the unfilled semi-crystalline films made from VICTREX™ PEEK polymer. The film provides a material solution for engineers in ultra-high performance applications.

APTIV films are a comprehensive range of versatile, high-performance films, the use of which can facilitate reduced systems costs, improved performance and enhanced design freedom.

APTIV 1000 has a unique combination of properties providing high temperature performance, light weight, mechanical strength, durability, excellent radiation, hydrolysis and chemical resistance, electrical insulation, wear and abrasion resistance, excellent barrier properties with high purity, good flammability without the use of flame retardants, low toxicity of combustion products, and low moisture absorption in a film format. Inherently halogen free and ease of processing makes APTIV films a technology enabler for our customers and end users.

Material Properties

Physical	Nominal Value	Unit	Test Method
Density (23°C)	1.30	g/cm³	ISO 1183
Water Absorption [1]			ISO 62
Equilibrium, 23°C, 0.0500 mm, 50% RH	0.040	%	
ShrinkageMD [2] (200°C, 50.0 µm)	< 0.50	%	
ShrinkageTD [2] (200°C, 50.0 µm)	< 0.50	%	
Films	**Nominal Value**	**Unit**	**Test Method**
Film Thickness - Recommended / Available	8 to 750 µm		
Tensile Modulus			ISO 527-3
MD : 23°C, 25 µm	2600	MPa	
TD : 23°C, 25 µm	2800	MPa	
MD : 23°C, 50 µm	2500	MPa	
TD : 23°C, 50 µm	2500	MPa	
MD : 23°C, 125 µm	2400	MPa	
TD : 23°C, 125 µm	2300	MPa	
MD : 23°C, 250 µm	2300	MPa	
TD : 23°C, 250 µm	2300	MPa	
Tensile Stress			ISO 527-3
MD : Break, 23°C, 25 µm	140	MPa	
TD : Break, 23°C, 25 µm	120	MPa	
MD : Break, 23°C, 50 µm	130	MPa	
TD : Break, 23°C, 50 µm	120	MPa	
MD : Break, 23°C, 125 µm	120	MPa	
TD : Break, 23°C, 125 µm	120	MPa	
MD : Break, 23°C, 250 µm	110	MPa	
TD : Break, 23°C, 250 µm	110	MPa	

E. Matlab code

```
%% Import .tra/.txt file
clear; clc; close all;

%A = importdata('3Dsys_200L10H3_real_sim.txt');
A = importdata('23_04_2026 3D 3xL6H2_2.TRA');

%% ========== Define maximum displacement for compression ==============
d_max = 7.9; % mm, adjust as needed based on the measurements
% ====================================================================

% Offset value if it doesnt start on y=0
y_offset = -0.0;
x_offset = 0;

%% Begin analysis

if isstruct(A)

    % Case 1: normal numeric data exists
    if isfield(A,'data') && ~isscalar(A.data)
        numericData = A.data;

    % Case 2: broken import (data = 1, actual data in textdata)
    elseif isfield(A,'textdata')
        rawData = A.textdata;
        % Remove first row (header)
        rawData = rawData(2:end, :);
         % Keep only first 2 columns
        rawData = rawData(:,1:2);
        % Convert to char/string safely
        rawData = string(rawData);
        % Remove leading/trailing whitespace
        rawData = strtrim(rawData);
        % Remove any non-numeric characters except . - + e E
        rawData = regexprep(rawData, '[^0-9eE\+\-\.]', '');
        % Convert to double
        numericData = str2double(rawData);
    else
        error('No usable data found.');
    end

else
    numericData = A;
end


%% Extract columns
force = numericData(:,1);
displacement = numericData(:,2);

% Compute change in displacement
delta_disp = [0; diff(displacement)];  % first element = 0

% Create a mask: include points that are either increasing or essentially
% flat
tolerance = 1e-4;  % threshold for ignoring tiny decreases
delta_mask = delta_disp >= tolerance;

% Combine with max displacement condition
```

```
idx_comp = (displacement <= d_max) & delta_mask;

% Apply mask
force_comp = force(idx_comp);
displacement_comp = displacement(idx_comp);
% force_comp = force;
% displacement_comp = displacement;

%% Optional: smooth the curve using moving average or interpolation
windowSize = 50; % adjust for smoother curve
force_smooth = movmean(force_comp, windowSize);


%% Create figure (Single-column journal size: 8.5 cm width)
figure('Units','centimeters','Position',[5 5 12 8]);
set(gcf,'Color','w');
hold on

figure(1)
set(gcf,'Units','centimeters','Position',[5 5 12 8]);
set(gcf,'Color','w');

%% Plot
xmin = 0;
xmax = d_max;
idx = displacement_comp >= xmin & displacement_comp <= xmax;
%idx = displacement >= xmin & displacement <= xmax;

% Main data plot
xlim([xmin xmax]);
plot(displacement_comp(idx) + x_offset, force_smooth(idx) + y_offset,...
    'LineWidth', 1.2);
%plot(displacement(idx) + x_offset, force(idx) + y_offset,...
    % '-.', 'LineWidth', 1)
hold on

%% Axis formatting (journal clean style)
set(gca,...
    'FontName', 'Times New Roman',...
    'FontSize', 9,...
    'LineWidth', 0.8,...
    'TickDir', 'in',...
    'TickLength', [0.015 0.015],...
    'Box', 'on');

xlabel('Displacement (mm)','FontSize',9);
ylabel('Force (N)','FontSize',9);

%% Zero Baseline (yline)
set(gca, 'LineWidth', 0.6, 'Box', 'on');
yline(0, '--', 'Color', [0.4 0.4 0.4], 'LineWidth', 0.4, ...
    'HandleVisibility', 'off');


%% ========== Legend =============

lgd = legend('b = 2.5 mm','b = 2.0 mm','b = 1.0 mm');

set(lgd, ...
    'Interpreter', 'tex', ...   % Ensures font properties are used
    'FontName', 'Times New Roman', ...
```

```
    'FontAngle', 'italic', ...  % Makes it italic
    'FontSize', 9, ...
    'box','off');


%% Create FEA vs Experimental legend
h_exp_style = plot(nan, nan, '-k', 'LineWidth', 1, 'HandleVisibility', 'off
    ');
h_num_style = plot(nan, nan, '-.k', 'LineWidth', 1, 'HandleVisibility', '
    off');

ax2 = axes('Position', get(gca, 'Position'), 'Visible', 'off');
hold(ax2, 'on');

lgd2 = legend(ax2, [h_exp_style, h_num_style], {'Experimental', 'Numerical'
    }, ...
    'Location', 'southwest');

set(lgd2, ...
    'Interpreter', 'tex', ...   % Ensures font properties are used
    'FontName', 'Times New Roman', ...
    'FontAngle', 'italic', ...  % Makes it italic
    'FontSize', 9, ...
    'box','on');

%% Reduce white margins
 set(gca,'LooseInset', max(get(gca,'TightInset'), 0.02))

%% Export clean vector PDF
exportgraphics(gca,'3D_L10H3_full2.pdf','ContentType','vector');
```

F. Literature review

Literature Review

by

Arturas Kiselis

Faculty of Mechanical Engineering
Department of Precision and Microsystems Engineering (PME)
2025

Supervisor: Dr. ir. Marcel Tichem

Abstract

This literature review covers state-of-the-art 3D multistable passive mechanical metamaterials based on bistable unit cells and evaluates their suitability for fabrication at the microscale using the MECOMOS method. Firstly, an in-depth overview of bistability and snap-through mechanics is presented. The performance of mechanical metamaterials is assessed through geometric parameters, deformation sequence and unit cell topology. Numerous existing 3D lattice metastructures are then collated, categorised, and presented, showing general trends and limitations in fabrication. Combination the most recent findings demonstrate that no scaling constraints exist due to the geometric nature of the unit cell and the total architecture. However, most existing 3D designs are limited to single DoF systems produced through conventional additive manufacturing, which introduces significant scaling challenges. Therefore, the findings reveal a critical gap between theoretical scalability and practical fabrication capabilities. In the context of the MECOMOS project, this highlights the need for more advanced and reliable microscale fabrication methods for 3D multi-DoF multistable motion systems.

Contents

Page

1 Introduction **1**
1.1 Scope . . . 1

2 Passive Metamaterials **3**
2.1 Bistable unit cells . . . 3
2.2 Bi-stability and snap-through . . . 5
2.3 Performance tuning . . . 7
2.3.1 Geometric parameters . . . 7
2.3.2 Deformation sequence . . . 9
2.3.3 Topology . . . 10
2.3.4 Bi-material composites . . . 11
2.4 3D Lattice Metastructures . . . 12
2.5 Stability configurations . . . 16

3 Fabrication **18**
3.1 Forming . . . 19
3.2 Laser machining . . . 21
3.3 Joining . . . 21
3.3.1 Solid state . . . 22
3.3.2 Soldering and brazing . . . 22
3.3.3 Fusion bonding . . . 23
3.3.4 Adhesive bonding . . . 24

4 Multistable system **25**
4.1 Mechanics . . . 25
4.2 Development and fabrication . . . 26

5 Conclusions **29**

1 | Introduction

For the longest time the mechanical behaviour of materials has been predetermined by their chemical composition and internal structure. However, in the past few decades with the advent of scientific breakthroughs and advanced manufacturing techniques, new materials, called metamaterials, have been created bypassing natural limitations and exhibiting properties absent in nature. Metamaterials, by definition, are artificially structured materials whose macroscopic properties result from their engineered microstructure rather than their base material composition demonstrating any desirable electromagnetic, acoustic or mechanical property as well as exhibiting negative mass, stiffness or Poisson's ratio under specific circumstances [1–4]. In addition, due to significant advancements in additive manufacturing (AM) technologies, the creation of such novel structures has become more efficient and affordable. In turn, this allowed engineers to exploit the unique properties and create bespoke designs and solutions for problems that would be extremely difficult using conventional methods. In the past two decades research of metamaterials has been focused mainly in optics, acoustics and thermal applications allowing the development of unique metamaterials like the perfect lens [5]. More recent advancements in the design, structural analysis and manufacturing technology facilitated development of high-performance sensors for pneumatics, load and thermal actuators [6].

1.1 Scope

The scope of this review and the MSc project will be limited to passive multistable mechanical metamaterials. In literature, mechanical metamaterials are classified in various ways; however, they follow a general structure throughout which usually includes metamaterial application, functionality and a basic structural composition of the unit cell (UC) [7, 8]. Based on their displacement type, mechanical metamaterials can be actuated either passively or actively. Actuation of the passive metamaterial is described via internal pre-determined structure which cannot be altered in post-fabrication. Thus, multistability is controlled by the variation in stiffness and snap-through instability through geometric properties. On the contrary, active metamaterials are activated via external stimuli. That is, they have the same initial structure as passive metamaterials, however, during the post-processing their deformation is further controlled via electricity, heat or light. In this work, passive metamaterials and their structures are of interest, thus, focus will be in that direction.

Unique designs of bistable UCs are the basis of every metamaterial which can be composed of origami, Euler's beam, shell surface or other [1] and exhibit mechanical traits like elastic buckling, multistability, and negative stiffness [7]. Metamaterial pie chart, combining all of these definitive properties, is depicted in Figure 1.1. Use of metamaterials has exploded in recent decades where more advanced applications are gaining more attraction compared to most basic functionality like energy absorption or dissipation. Those are used in sensor technologies and robotics, vibration control, actuators, intelligent biological systems or wave control for optics and physics.

Moreover, the aim is to fabricate a 3D multi-DoF system to demonstrate functionality applying the MECOMOS (Mechanical metamaterials for Compact Motion Systems [9]) method researched at TU Delft. Thus, two research questions are raised ***What geometric param-***

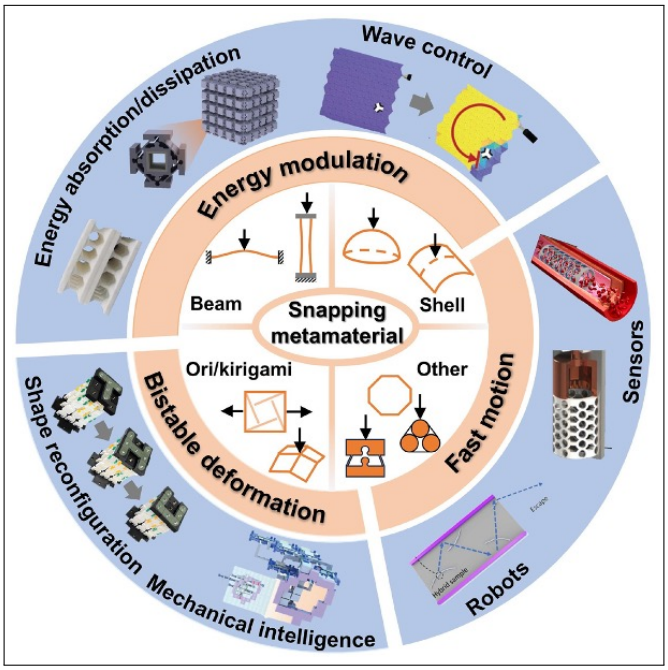

Figure 1.1: Chart displaying classification, functionalities, and potential applications of snapping mechanical metamaterials [8].

eters determine multistablity of the metastructure? and ***How current micro fabrication techniques in relation to the MECOMOS affect design and mechanical performance of stacked multistable metastructures?*** Although these questions may seem unclear at first, they will become clearer as the subsequent findings are presented.

The structure of this report will be as follows. Chapter 2 will give an in-depth overview of the mechanics behind bistable and multitstable materials including force-energy displacements, topological relationships, deformation sequence and other multistability performance parameters. Examples of state-of-the-art passive metastructures available in the literature will be presented including their technical parameters. Chapter 3 will cover current micro-fabrication techniques. Topics like polymer µ-forming, laser machining and µ-joining will be discussed. Finally, chapter 4 will combine knowledge gained from chapters 2 and 3 by discussing the mechanics and manufacturing feasibility of micro-scale multistable metamaterials. In this way, a better understanding and the overview of the project will be reached concluding the design viability. Noteworthy, although metamaterial scientific research has been active for over several decades, the time frame for publications has been chosen as 2016-2025 to narrow down to more relevant findings for this review.

2 | Passive Metamaterials

This chapter will cover theoretical background behind the bi-stability and snap-through induced deformation and its phenomena. The snap-through instability will be considered from the force, energy and displacement perspective as well as via conditions required for two distinct equilibrium states. Passive programmability subsection will cover analytical and mathematical relationships required for the bistability of passive metamaterials. Furthermore, general categories and examples of bistable UCs will be introduced that have been widely covered in the literature. Following the scope of this review, focus will be gradually shifted to unique tessellated and stacked 3D metamaterials that have been realised through beams, shell structures or combination of both to achieve desired functionality.

2.1 Bistable unit cells

Bi-stability of an element can be achieved through multiple types of UC structures as indicated in the previous chapter Figure 1.1. Generally, snapping metamaterials can be classified into three categories. Those are bistable beams, shell-like structures (including origami and kirigami) and other unique structures [7, 10–13]. N.B. Some research literature separates shells and ori/kirigami into two distinct categories as they carry slightly different structures [8, 14]. In essence, all of these mechanical structures achieve bistability and have two equilibrium states through snapping instability. A tabulated visual description is shown in Figure 2.1.

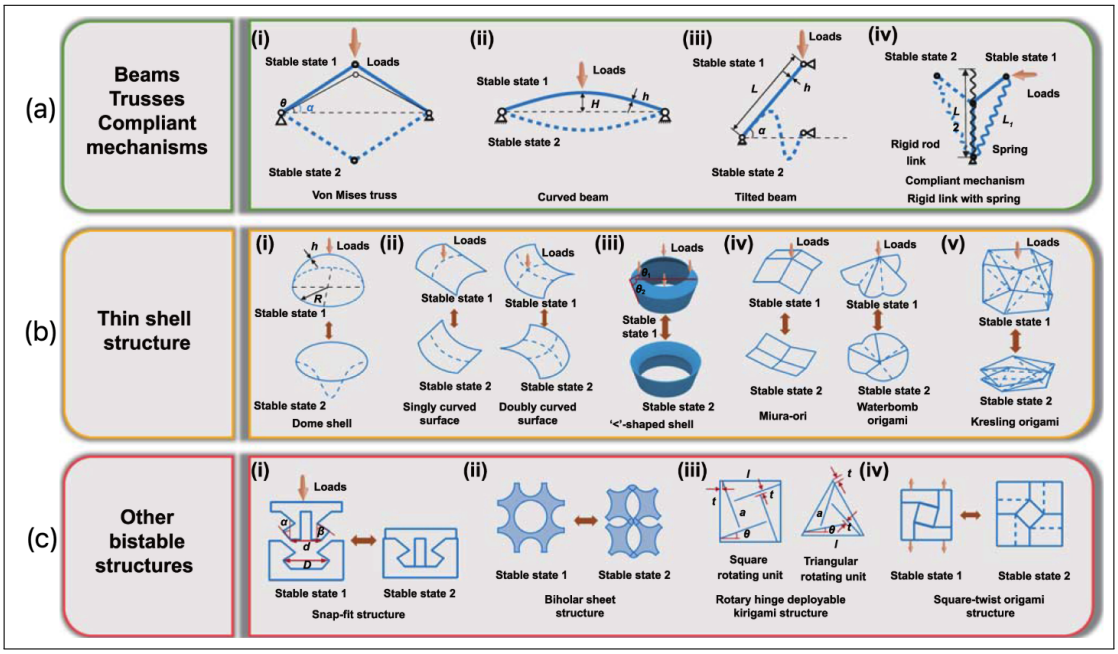

Figure 2.1: Common bistable units. **(a)** Bistable beams, truss units and compliant mechanisms. **(b)** Bistable shell-based and ori/kirigami structures. **(c)** Other innovative bistable structures [13].

- **Beams-based structures:** These types of structures are the most basic in their mechanical structure and are easy to implement and manufacture. They have remarkable properties like variable equilibrium states, changeable bending stiffness, high robustness and other diverse functionalities [14]. It consist of (i) Von Misses truss, (ii) Pre-curved beams, (iii) Tilted beams (iv) compliant mechanism. Von Misses truss consists of two

beams connected at the center point and fixed (or pinned) at the other ends. Bi-stability properties and snap-through are purely derived from the hinged connection where beams themselves do not undergo mechanical deformation. Due to relatively small displacement they are often used in soft robotics wave control or mechanical logic operations [11, 13]. Pre-curved beams are double clamped and buckling induced bistable units due to applied horizontal force [15]. Monostability and bistability variations depend on the Q factor Equation 2.2 where symmetric snap-through behaviour is achieved. Tilted straight beams, contrary to vertical elastic beams that buckle under axial compression and are monostable, achieve snapping bistability by fixing one end and vertically displacing the other [16] and depends on the inclination angle α and K factor (Figure 2.1 a)).

- **Shell structures**
  - **Curved shell:** includes dome-like structures, cylindrical curved surfaces bent in one direction and double bent cylindrical plate. Bistability of curved surface UCs is highly controlled by relative thickness to length ratio. They are commonly integrated into various soft actuators for their bistable and multistable properties [11, 13]. On the other hand, dome-shaped shells deformation is similar to that of a buckling beam where snap-through transition transforms into either convex or concave shape. Stability and rate of this transformation depends on several factors like angular opening of the shell ϕ, dome thickness h and curvature radius R as ilustrated in Figure 2.1 b). Spherical dome surfaces are commonly used in soft robotics, energy absorption and wave control [17, 18].
  - **Conica frusta**: is a combination of conical shells by joining creases. Its deformation mode is similar to Von-Misses truss and connects compliant mechanisms with springs. Though, strength and stability of the structure are questionable where monostability and bistability properties of conica frusta depend on angles θ_1 and θ_2 [13].
  - **Origami/Kirigami:** More common surface-based snapping material includes Miura-ori, Waterbomb, Kriesling and curved crease origamis [8]. Through crease folding and deformation a 2D design can be transformed into a 3D structure. Similar to dome shells, these structures demonstrate bistability from concave and convex shapes due to deformable creases where surfaces stay rigid at all times. Notably, they can also serve as auxetic materials [10]. Full 3D cell structures can also be designed by stacking folded layers. Finally, Kirigami-patterned sheets can exhibit out-of-plane deformations due to cuts in their sheet structure enabling formation of complex 3D mesostructures [10, 19]. Application of these metamaterials is commonly seen in deployable devices, shape reconfiguration structures and similar.
- **Other innovative structures:** Design variations are much greater in innovative structures due to their unique cell design topology, although they are achieved by either modifying conventional structures or introducing new structures. This includes snap-fit structures, biholar sheets, tensegrity structures, granular metamaterials with multistability and other [20].

It is also worth noting that extensive literature reviews have been conducted based on the application and purpose of metamaterials which may possess bistability properties but do not conform to general definitions described above. This includes, but not limited to, electromagnetic, photonic, acoustic metamaterials as well as complex examples like frequency-selective

surface-based or local resonance metamaterials [1]. These atypical metastructures, however, are beyond the scope of this literature review but, nonetheless, have a significant importance in engineering research.

2.2 Bi-stability and snap-through

Mechanical metamaterials can exhibit multiple DoF to achieve desired action or function. Such freedom in metamaterials is explored through unique non-linear property of bi- and multi-stability. This means that the structure changes the shape due to a stable position of UCs through mechanical deformation. In other words, when a system stores and releases energy to achieve motion under continuous or step force input. On the other hand, snap-through is a geometric condition allowing quick system transition to either of the stable states [8, 11, 13, 21, 22]. A figure showing the snap-through mechanism (pre-curved beam) from stable state 1 to state 2 is presented in Figure 2.2. To demonstrate snap-through behaviour, a UC is ideally fixed on both ends where vertical force F is applied at the central location of the beam. If applied force exceeds critical threshold F_{cr}, beam snaps into the second stable state [13]. This critical force represents the buckling threshold of the structure and relates to the bearing capacity of the construction. Considering that the states are symmetrical, an equivalent reaction force is required to return to the original configuration (i.e., 1^{st} state). The deep orange line in Figure 2.2 b) indicates that the minimum force value drops below zero meaning that continuous energy input is not required to achieve either equilibrium states and thus, the 2^{nd} state is maintained. Notably, the negative force implies transition from the positive stiffness to the negative during the snap-through deformation. The energy-displacement graph confirms the presence of two equilibria by displaying one local maximum and two local minima in Figure 2.2 c) meaning that both states have different energy levels. Initially, a bistable element increases in elastic energy during the loading by reaching maximum value at snap-through point (peak). As soon as that point is reached, the structure releases the excess energy shown as $U_{release}$ when the second stable state is reached.

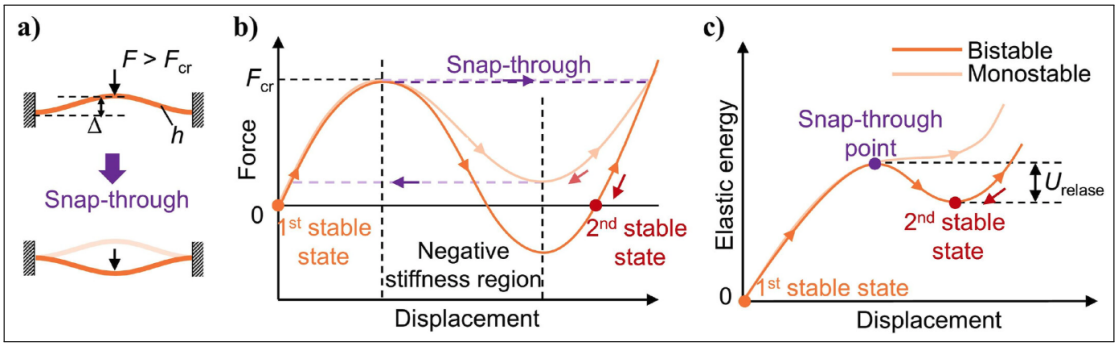

Figure 2.2: Snap-through instability for bistable and monostable behaviours of a negative stiffness mechanism. **a)** Schematic drawing. **b)** Force-displacement-graph. **c)** Energy-displacement graph. Edited from [8].

Contrary to bi-stability, as name suggests, monostable beam cannot sustain two equilibrium positions and returns to the first state as soon as the force is removed. The absence of snap-through instability is conveyed through light orange line where negative stiffness region is not reached Figure 2.2 b)). Elastic energy-displacement graph shows that as soon as snap-through

point is reached, removal of the force facilitates continuous energy rise of varying rate until returned to original 1^{st} state [8, 13, 22].

For 3D multi-stable metamaterials consisting of tessellated and stacked snapping units, snap-through behaviour has a direct impact on the energy dissipation capacity. In other words, mechanically stiffer UCs will lead to an improvement of metastructures' energy dissipation [23]. Such energy dissipation or trapping can be seen in force-displacement graph for lattice metamaterials shown in Figure 2.3. Three examples were taken to demonstrate energy trapping phenomena in such systems. Figure 2.3 a) and b) are beam type lattices whereas Figure 2.3 c), is a shell like structure. Clearly, due to negative stiffness, the graph shows distinct "jumps" or peaks in the force during cyclic loading and unloading (negative and positive force respectively). It is worth noting that these loading tests are quasi-static in nature to avoid any dynamic loads meaning that the force is gradually applied and any inertia in the structure is avoided. As the load is applied, all layers experience compressive deformation. Once the first layer collapses due to reached maximum load-bearing capacity, a sudden peak appears as shown in the response curve. Subsequently, the metamaterial enters the negative stiffness stage, and the deformation inside the metamaterial mainly occurs in the collapsing layer until the layer is completely compressed and enters the next deformation cycle [20]. Shaded areas indicate dissipated or trapped energy in the system. In the research it was observed that number of occurrence of snap-through behaviour (or peaks) and the maximum load, F_{max}, are not dependent on the number, type or overall size of the UCs per side but rather number of layers in the structure [24]. The more layers there are, the higher the number of snap-through "jumps". However, this sometimes can experimentally deviate due to material imperfections in the lattice leading to asymmetric deformation and weakening the snap-through behaviour [20]. Applying this unique characteristic of energy trapping in the system, multiple applications in engineering can be seen like energy storage, energy absorption and low-energy consumption [8, 13].

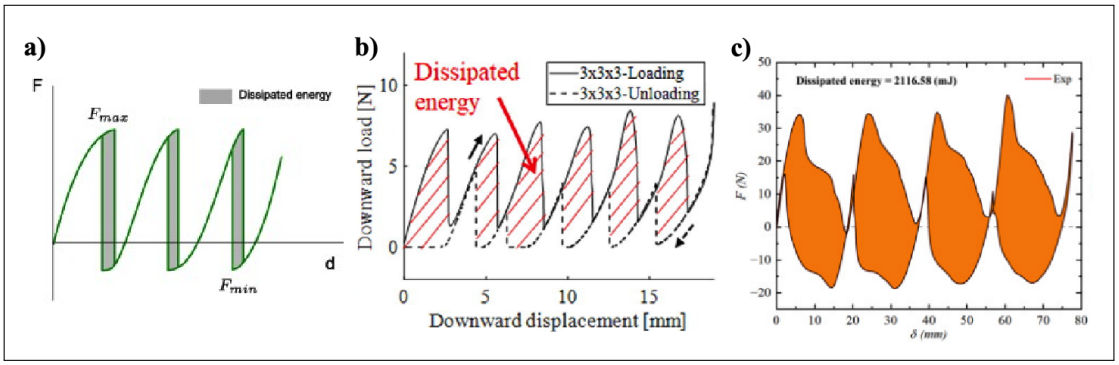

Figure 2.3: Load-displacement relationships of lattices comprising multiple bistable UCs in response to the cyclic loading. **a)** Three-beam system, adapted [23]. **b)** Tetra-beam-plate metastructure 3×3×3, adapted [24]. **c)** Square deep dome 2×2×4 arranged multistable metamaterial, adapted [20].

The snap-through sensitivity and rate of the response can be tuned by appropriately by adjusting the geometrical parameters, topology and/or basic material properties of the metamaterial UCs leading to multiple advantages like improved energy absorption and performance [25]. Although it is worth mentioning that the energy absorption mechanism stems solely from the structure's geometric snapping transformations and thus, loading rate has no effect [22].

2.3 Performance tuning

In the previous section, snap-through instability was discussed via force, energy and displacement perspective. To gain a better understanding of this phenomena, key governing mechanical characteristics of the snap-through transition will be presented and topology influence on the UC performance discussed.

2.3.1 Geometric parameters

A pre-curved cosine beam is a crucial element of the bistable behaviour which is dictated by multiple factors. Due to its nonlinearity, the mechanical response can be tailored by a proper choice of an elastic base material or even by appropriately adjusting the topological and geometrical design [22]. The initial configuration of the beam ($w(x)$) is mathematically expressed as

$$w(x) = \frac{h}{2}\left(1 - cos\left(\frac{2\pi x}{l}\right)\right) \tag{2.1}$$

where x represents horizontal coordinate along the span of the beam, l. Parameters t and b are in-plane and out-of-plane thickness while h is the height of the cosine-shaped beam as seen in Figure 2.4. The crucial importance of the Q factor was also identified in the mechanical behaviour of the bistable mechanism which is defined as

$$Q = \frac{t}{h} \tag{2.2}$$

Specific values of Q determine stability conditions having a significant effect on the normalized force–displacement curve i.e, when $Q > 2.31$ the beam is bistable, while $1.21 < Q < 2.31$ exhibits a snap-through monostability. Additionally, during transition, a curved beam experiences rotation at the midpoint leading to the second buckling mode. To counteract this unwanted phenomena, it was determined that the single beam must have a centre plunger attached or connect two curved beams together to prevent it from twisting [15]. Hence, all metamaterials based on a pre-curved beam are designed in such way that satisfies two bistability conditions: 1) large enough Q factor and 2) the second mode must be constrained [11, 26–28].

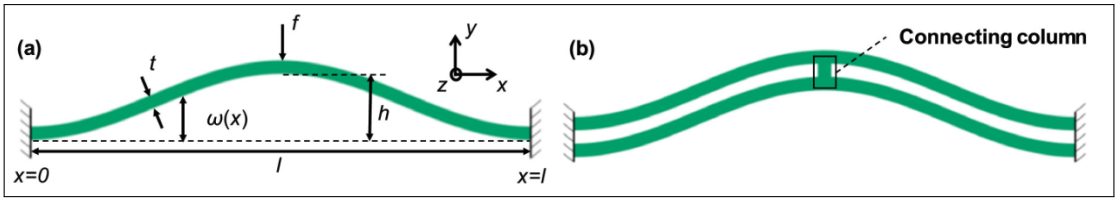

Figure 2.4: Geometric configuration and parameters of **(a)** the sinusoidal curved beam and **(b)** double curved beam design [27].

Now, some bistable beam metamaterials have advanced further than just standard pre-curved beam configuration which has introduced additional geometric factors, influencing the structural performance and the snap-through behaviour. As seen in Figure 2.5, it was identified that the snapping transition can be either self-recovering (monostable) or multi-stable depending on the relative thickness t_2/t_1 of the snapping and supporting segments as well as the amplitude

of the snapping curved segments b/l [21, 22].

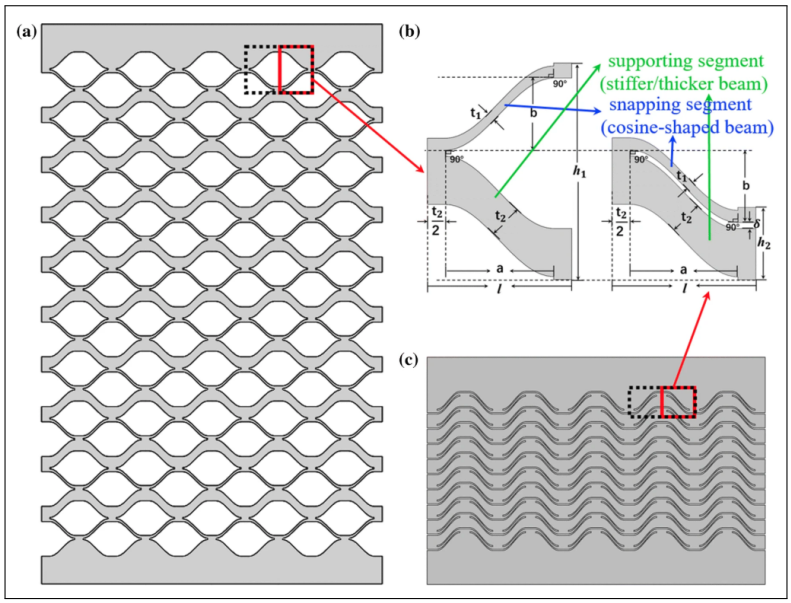

Figure 2.5: Mechanical metamaterial with parallel U-shaped snapping segments (PUMs). **a)** 5×10 stretched structure. **b)** Half of UC. **c)** Compressed structure [22].

Other important parameters influencing performance of multistable metamaterials was identified as the height-to-span ratio h/l and thickness-to-span ratio t/l. The former strongly influences multistability, i.e, by increasing h/l, the ability of the metastructure to sustain multiple stable configurations increases. On the other hand, t/l affects stiffness of the metastructure or how easy/difficult it is for a UC to transition into either of stable states [29]. Considering that metamaterials can exhibit the same behaviour at different design scales, a geometric similarity parameter, $P = l/h$, becomes essential for scaling designs to different sizes while keeping the same mechanical functionality [26]. Thus, it seems that there is a fine line in performance tuning of scaled UCs when considering its apex height, h and length, l. Finally, considering more unique UC designs that are inspired by inclined (tilted) slender beams, their snap-through response can be controlled by adjusting the beam slenderness ratio ($r_t/2r_b$) and the inclination angle, α as shown in Figure 2.6 a) [24]. However, tilted beams have shown an inferior mechanical response compared to cosine shapes which can provide a wider parameter range to achieve bistable behaviour. Observed that mechanical properties like strength, energy trapping property, and stiffness magnitude variation are also greater in cosine beams [30].

Geometric parameters of dome UCs follow the exact pre-curved beam equation as per Equation 2.1 since revolving the same beam around its axis results in a solid shell design where the same geometric relationships govern bistable response as shown in Figure 2.6 [20, 31–33]. Nonetheless, compared to shallow dome designs, deep domes are not only sensitive to h/t ratio but also to h/l ratio which proves increased sensitivity of deep bistable square domes [20]. In spherical shells, stability and rate of this transformation depends on several factors like angular opening of the shell α, dome thickness h and curvature radius R. It is worth noting that geometric parameters of unique UC designs and perfectly spherical dome shells are difficult to compare against the conventional pre-curved beam or dome structure due to a complex

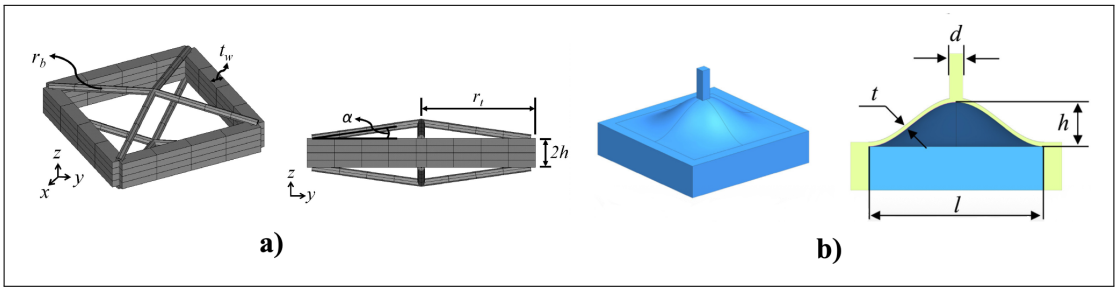

Figure 2.6: **a)** Tetra-beam-plate UC (tilted beams) with geometric parameters [24]. **b)** Deep dome shell with geometric parameters [31].

topology or scarcity of multistability examples and thus, are not considered for this review.

2.3.2 Deformation sequence

If the metamaterial consists of identical UCs, the sequence of stable configurations that metamaterial transitions to in response to a given force input is unpredictable [34]. In energy absorption applications, such uncertainty characteristic may not be an issue, however, that is not the case in areas where a deterministic deformation sequence is preferred e.g., precision alignment. By varying the thicknesses or initial shapes of the curved segments of the UCs, minimum and maximum F_{cr} can be tuned and thus, a deterministic transition achieved. Subsequently, the larger critical force will lead to a higher strain energy for that UC.

The first method is by varying the beam thickness t from row-to-row starting from 0.9 mm to 1.15 mm by 0.06 mm increments as shown in Figure 2.7 a). It was observed that the experimental row collapse sequence (1→5→4→3→2) was in good agreement with predicted FEA and numerical models which correspond to the thickness variation ($t_1 < t_5 < t_4 < t_3 < t_2$) respectively. The second method is variation in the mode imperfection size α_3 of the initial pre-curved beam. Although it is not explicitly stated in this literature review but factor α_3 is closely linked to Equation 2.1 the third-buckling mode. Again, the same collapse sequence was achieved as with thickness variations. Although research was conducted on a model with the small number of UCs and with simple variations in parameters, it is assumed to be valid for complex metamaterials with a large number of UCs and spatial variations [34].

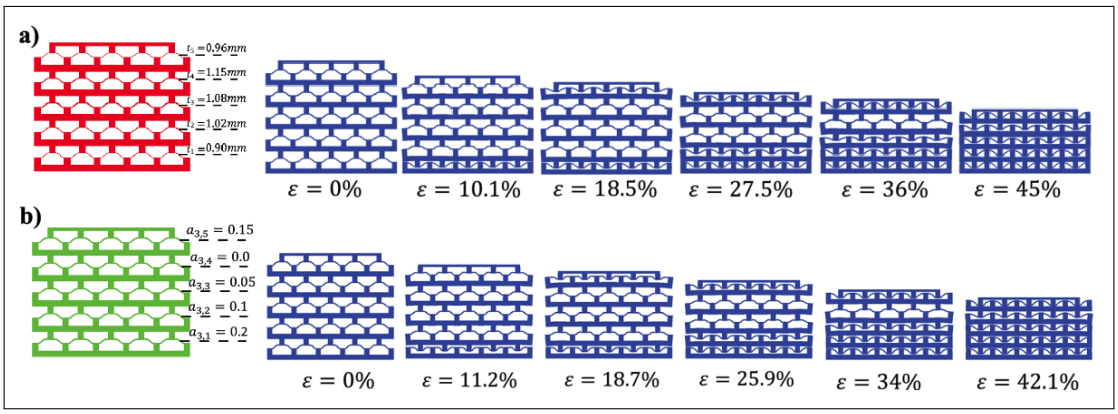

Figure 2.7: Deterministic collapse sequence of the 5×5 multistable metastructure. a) Thickness variation t. **b)** 3^{rd} mode shape imperfection adjustment a_3, adapted [34].

Similarly, deformation sequence in some cases with unique spatial variations is demonstrated as shown in Figure 2.8 a). Instead of adjusting the beam thickness t, sequential deformation can be achieved via pre-curved beam out of plane width, b and the total number of beams per layer, n which are directly proportional to F_{cr} of the each level. Furthermore, in deep square domes controlled collapse sequences can be achieved by adjusting the thickness or height of the UCs in different layers [20].

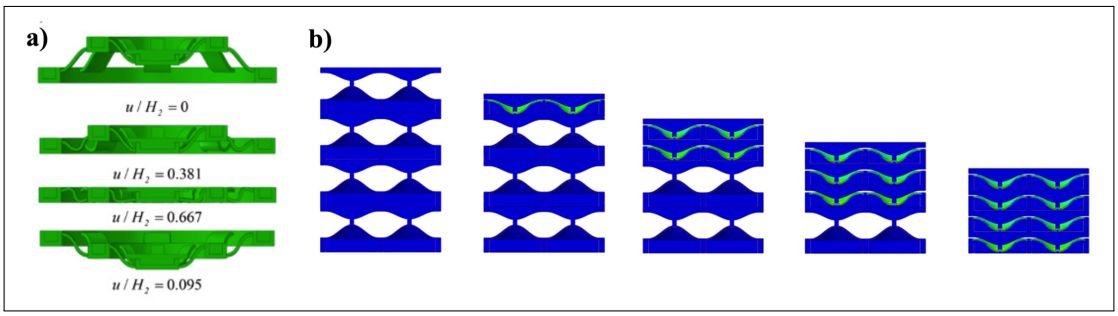

Figure 2.8: **a)** Deterministic collapse sequence of the cone metastructure [25]. **b)** Deterministic collapse sequence of the $2 \times 2 \times 4$ square deep dome metastructure [20].

Thus, depending on the beam configuration and 3D construction of the metastructure, multiple factors impact sequential deformation. Ultimately, everything relates back to the critical force F_{cr} which determines transformation sequence of a certain layer. Interestingly, it was analysed that the influence of loading rate on the deformation sequence is insignificant as the snapping force will generally increase by uniformly distributing throughout all rows which has been confirmed by force-displacement plots. This suggests that the collapse sequence is determined by the composition of the buckling element and not the load rate or support structure around it [35].

2.3.3 Topology

Besides geometrical parameters mentioned in the previous section, a UC topology influences multistability as well as energy storage. Generally, most designs are based on solid pre-curved beams, however, exploring modified topology provides an interesting insight into the total performance of the system.

In the literature it has been found that the very basic adjustment of UC dimensions is extremely effective in comparison to the traditional bistable UC structure with the uniform curved beam. Maintaining the same maximum strain during the snap-through deformation process, simply adjusting the width of the UC beam has shown to improve peak force by 155%, negative force by 91% and energy absorption by 136%. Furthermore, quasi-static FEA tests have been conducted on multilayer multistable structures where force-displacement curves have shown major improvements in the energy absorption [36].

Having the full tunable control over tailored bistable cells with precisely controlled maximum instability forces can be advantageous whilst constructing a multistable mechanical metamaterial. UC designs with unique surface topologies can enable gradient snapping sequences and deformation models for various 3D lattice structures. Presented in Figure 2.9, researchers per-

formed topology optimization on the pre-curved beam surface for specific maximum instability forces [37]. Obtained results were in good agreement with experimental quasi-static tests which subsequently proved effective regulation of the peak instability force f_e allowing greater fine tuning. Further, it was expanded onto designing a stacked metamaterial and 3D construction where results showed good capabilities of precise control over collapse gradient characteristics.

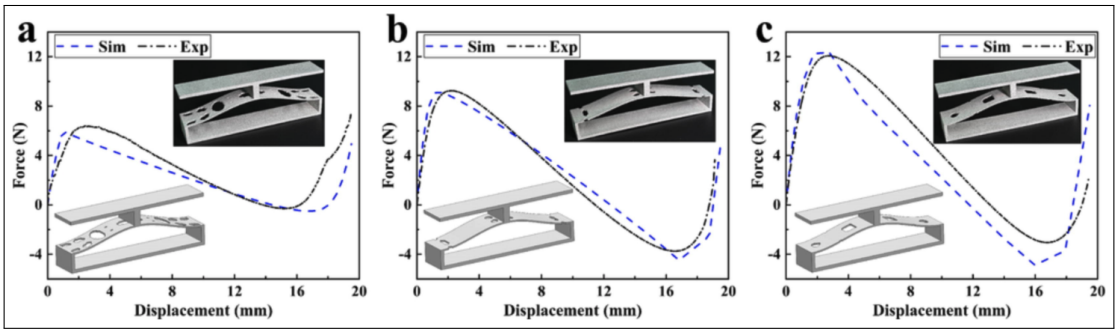

Figure 2.9: Results of optimized UC designs with heir respective force−displacement diagrams. Expected instability forces are: **a)** $f_e = 6N$ **b)** $f_e = 9N$ **c)** $f_e = 12N$ [37].

Considering the energy dissipation of multistable metastructures, solid beam designs exhibit relatively low performance. To counter that, two unique structural designs have been proposed as building blocks for multi-stable metastructures. These are lattice and hollow cross-section designs [23]. Results from numerical and experimental testing showed that the force required to achieve a snap-through behaviour was larger which indicates a higher energy storing capacity. Moreover, the multistability performance was influenced not only by the coefficient Q but also depended on the distance between the top and bottom skin T_v for lattice design as well as the thickness of the side wall, t_1 in hollow beams as shown in Figure 2.10 a) and c). Experiments of combined UCs into a five-layer structure showed that indeed, novel designs have yielded a uperior energy storing capacity due to enhanced bending stiffness subsequently requiring more force to achieve the second equilibrium state of the UC. A concept of lattice beam was also expanded into a shell design where it was theorised that energy dissipation can be effectively improved by achieving a stiffer mechanical response compared to solid shell designs [23]. Regardless of these results, fabrication in smaller scales requires more precision and thus, choosing an appropriate fabrication method is crucial.

2.3.4 Bi-material composites

Generally, multistable metastructures are designed from a single uniform material and, where necessary, made thicker if additional stiffness is required at the supports or the base. Although this method provides enhanced snap-through in monolithic structures, to achieve a completely symmetric snapping, thick fully fixed constrains at the ends of the snapping segments are required. Hence, this leads to less efficient usage or waste of the material. As an alternative, bi-material or multimaterial examples are explored where support structure is made from a stiffer material compared to buckling elements. One of the first innovative designs have shown that a stiffer support material made from GBR-PA12[1] leads to reduced lateral deformation during the dynamic loading and achieved enhanced snap-through transition based on force-displacement

[1] Glass beads reinforced polyamide 12

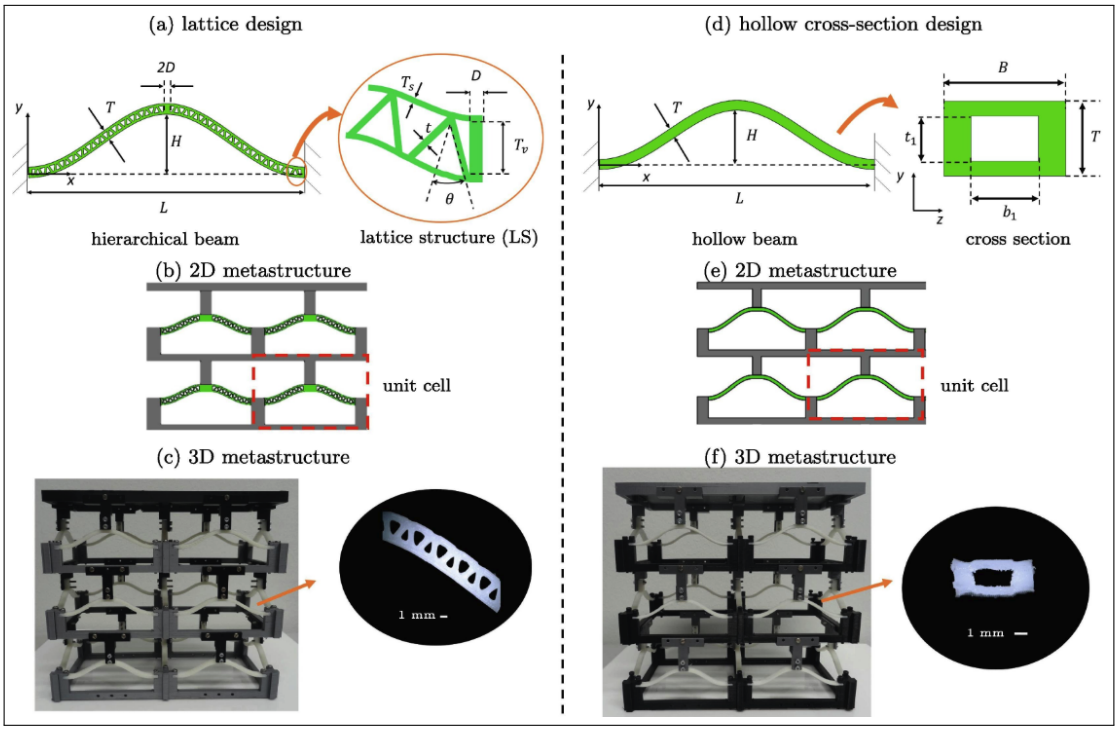

Figure 2.10: As schematic of proposed bistable UC designs. **a)**−**c)** Bistable lattice cell topology. **d)**−**f)** Box-shaped cell topology [23].

plots [35]. Further, research was conducted using combination of bi-material design PA-HIPS[2] which resulted in an enhanced impact resistance and energy absorption capacity compared to the mono-material lattice made just from PA. However, despite these advantages, reduced recoverability due to increased local plastic deformation at joints was observed [28]. Additionally, substitution of TPU with a stiffer material PLA to enhance the stiffness of a specific section of the structure resulted in increased critical loads F_{max} and F_{min} of the UC proving that the dual material design allows further enhancement of the specific energy absorption [38]. Despite these positive improvements compared to mono-material designs, more research is required to establish any reliable conclusions.

2.4 3D Lattice Metastructures

Tessellated UCs can be combined into a single planar surface design or a lattice structure. For this literature review, a combination of such periodically repeating layer of bistable units can be referred as *metasurface*. Although noteworthy, the definition of a metasurface in engineering community usually refers to a 2D planar surface (subwavelength thickness) with unique electromagnetic and photonic properties [39, 40]. In this review however, definition of a metasurface is assumed to be a 2.5D surface which contains bistable UCs and is within sub-centimetre scale as illustrated in Figure 2.11. Here, bi-stability and snap-through deformations of planar metastructures are greatly explored in the literature whereas 3D lattice formations of such structures are relatively sparce.

The following table (Table 2.1) will present 3D lattice passive metastructures which have been

[2]HIPS - high impact polystyrene.

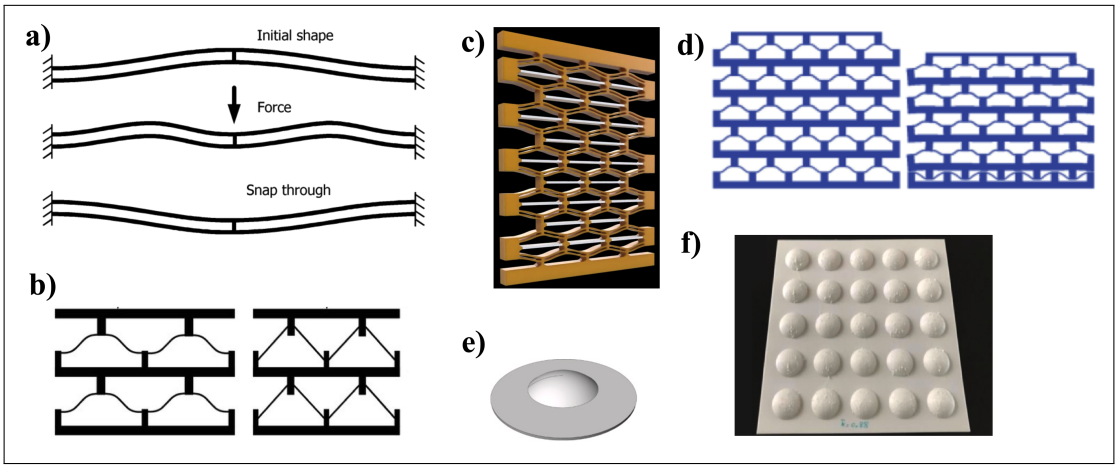

Figure 2.11: 2D beam and spherical metamaterials. **a)** Bistable double curved beams, adapted [15]. **b)** Multistable 2D beam/truss-based structures, adapted [11]. **c)** Multistable metamaterial arrangement of curved double beams, adapted [28]. **d)** Multistable metamaterial, adapted [34]. **e)** Spherical dome shell model isometric view, adapted [41]. **f)** The natural (undeformed) state of the sheet with natural dimples on a square lattice, adapted [18].

stacked to obtain multi-degree freedom. Three common bistable UC categories have been categorised which are: beams and trusses, spheres and domes and other unique cell designs. It is worth mentioning that each UC category contains distinct examples of non-repeating architecture to show design variety found in the literature. The table also includes metamaterial features like degrees of freedom of the whole structure, fabrication method, material and UC size. Lastly, footnotes were added for clarification on certain materials and fabrication methods.

Taking a closer look at the Table 2.1 results, most systems exhibit only 1 degree of freedom (DoF). It can be assumed that this way testing is simplified and focus can be shifted to observation of mechanical behaviours, snap-through phenomena and energy dissipation. In a way, having one or three translation directions would still yield the same mechanical response. Moreover, tests on such 3D structures are conducted under quasi-static loading and thus, having an extra rotation or translation freedom could lead to the undesired additional inertia in the system. Some cases e.g., shell-like structures [33, 42] have virtually infinite DoF due to their flexibility and testing conditions. Considering fabrication methods of these lattice metastructures, fused deposition modeling (FDM) is by far the most common approach since it provides a quick and easy way of producing a uniform prototype without requiring complex manufacturing techniques. Although, some examples present perfectly functional selective laser sintering (SLS) or stereolitography (SLA) printed structures, there was no clear indication why these methods were preferred over the FDM. Notably, unique fabrication methods like the two-photon polymerization (2PP), laser cutting, gel casting and injection moulding were also used due to extremely small size of the test model [43], bi-material construction [44] or complex architecture of the metamaterial [33].

Table 2.1: Overview of 3D lattice multi-stable metastructures

UC type	DoF	Fab method	Material	UC size [mm]	Figure	Ref.
Beams and Trusses	1	SLS	PA	23 × 23 × 8.2	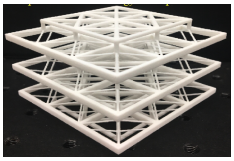	[24]
	1	FDM	TPU[3]	74 × 74 × 47		[25]
	3	MJF	PA	50 × 10 × 5	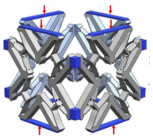	[37]
	1	2PP	IPS[4]	0.865 × 0.865 × 0.38	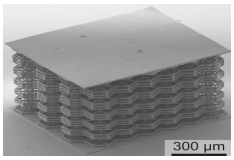	[43]
	4	Laser[5]	301 SS[6]	73 × 73		[44]
	1	SLA	PA	60 × 15 × 12	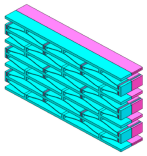	[45]
	1	FDM	TPE	14.8 × 14.8 × 3.6	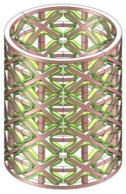	[46]
	1	Water-jet	304 SS	56 × 5.6 × 1.4	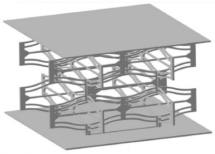	[47]

Continued on next page

[3]The flexible buckling elements are made of TPU and the rigid elements are made of PLA.
[4]A photoresist resin.
[5]Snapping elements laser cut and supports FDM printed.
[6]PLA supports and SS (AISI 301) snapping elements.

UC type	DoF	Fab method	Material	UC size [*mm*]	Figure	Ref.
	2	FDM	PU	10 × 40 × 35		[48]
Domes and Spheres	1	FDM	TPU[7]	40 × 40 × 15	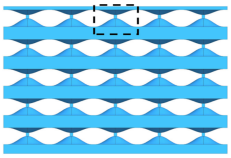	[20]
	1	FDM	PLA-ST[8]	120 × 4.5 × 5	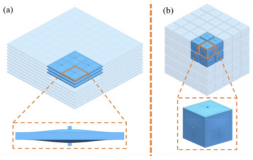	[31]
	1	FDM	ABS	R50 × 5.5	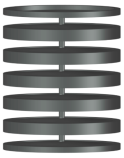	[32]
	1	Gel-cast[9]	PU[10]	R10 × 3		[33]
	-	FDM	TPU	R8 × 4.8		[42]
	1	Gel cast	Sylgard 184	R10 × 6	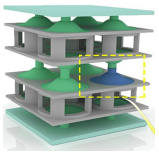	[49]
Other	3	SLS	TPU	50 × 50 × 50	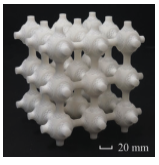	[50]

Continued on next page

[7]Shore hardness 95A.
[8]Super-tough PLA.
[9]SLA printed molds for gel-cast and FDM base.
[10]PU for single layer structure and TPU for the base.

UC type	DoF	Fab method	Material	UC size [mm]	Figure	Ref.
	1	Injection moulding	TPU	R47 × 10		[51]
	1	SLA	-	R5 × 100		[52]

To demonstrate functionality, researchers commonly use polymers for their prototypes, such as polyurethane (PU) and thermoplastic polyurethane (TPU). Due to their availability, high material strength and compliance, they are generally the preferred materials to work with. They are also easy to use with 3D printing systems and allow straightforward comparison of force– and energy–displacement data with previous works. Considering the UC sizes, they all range within the centimetre scale. Every UC, with the exception of the square dome [31], is no larger than 80 mm in length, which is sufficient to demonstrate energy absorption capabilities but challenging for high-precision applications, where sub-centimetre designs are preferred.

2.5 Stability configurations

It was mentioned before, most of the 3D lattice metastructures exhibit a one degree of freedom (1 DoF) during vertical quasi-static load tests and are limited to translational state changes. This behaviour can be attributed to the inherent constraint of UCs' rotational compliance, although a very few examples are available of such phenomena [48]. This can also be attributed to the application conditions, where partial UC engagement during loading results in reduced energy absorption. However, considering these limitations, especially lack of rotational compliance, some examples in the literature demonstrate a new type of three-dimensional (3D) multi-stable metastructure enabling both level and tilted stable configurations in addition to other equilibrium states [29, 44]. Combined into a 2D array, bistable units can morph top surface into a wave like pattern and create multi-stable surface designs also called mesostructure-based surface offering more design freedom for motion-related applications as seen in Figure 2.12.

When deformed, two configurations are distinguished: level stable configuration (LSC) and tilted stable configuration (TSC). It was found that the TSC contains higher strain energy after transition leading to lesser stability compared to the LSC. In other words, a tilted configuration is more likely to snap back into the original state compared to the level configuration. Depending on the general structure of the metamaterial, stacking n layers of bistable elements with x stable configurations results in a metastructure with x^n stable configurations including parallel and hybrid states [44]. Application of such mechanical phenomena has great potential in surface morphology where variety of stable states results in unique surface patters like corrugated sheet design as shown in Figure 2.12 c). The multiplicity of surface morphology can also

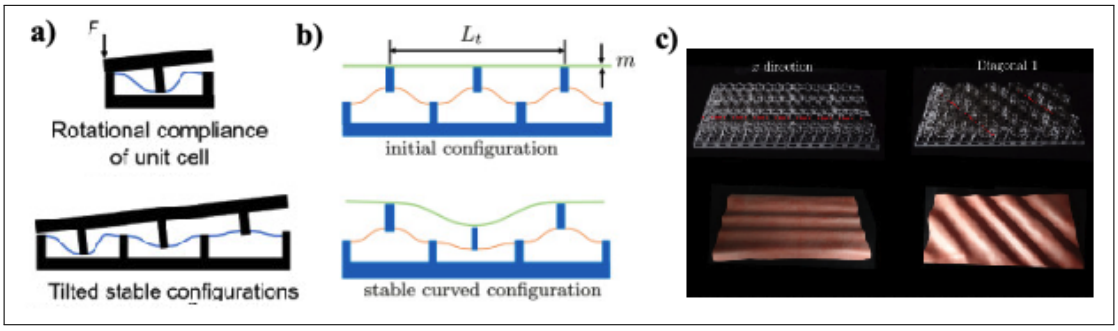

Figure 2.12: Morphing surface design. **a)** Schematic of a multi-stable metastructure exhibiting level stable configurations and rotational compliance, adapted [44]. **b)** and **c)** Composition of three bistable elements. When the center element snaps, the attached plate (green) can stabilize at the curved configuration, leading to multi-stable mesostructure-based surface, adapted [29].

be useful in morphing airfoils or adaptive optics where novel compliant surface-tunable mirrors can be used for distorted wavefront correction [29].

To conclude this chapter, mechanics of bistable unit cells and behaviour of the 3D multistable mechanisms has been reviewed. It was analysed, that the multistability is driven by geometric factors as well as topological modifications to achieve desirable displacements and energy modulation. By providing theoretical basis for the unit cell design, the next chapter will cover fabrication methods necessary to realise the system at the microscale.

3 | Fabrication

Some may argue that the fabrication of metamaterials is more challenging than their design. Although theoretical knowledge and use of mathematical models enables scientific creativity in design stages, fabrication and actual realisation of multiple complex architectures with designated functionality is dictated by current manufacturing technologies. Manufacturing accuracy and resolution has significant impact on metamaterial inherent structure and performance. In recent decades additive manufacturing (AM) has gained significant traction due to multiple of reasons. AM exceedingly outperforms in flexibility and architectural resolution bandwidth compared to the subtractive manufacturing (SM). Due to intricate design of mechanical metamaterials, AM has become extremely common fabrication method enabling fast and efficient results. There are over 20 types of AM techniques ranging from a few nanometre to centimetre resolution with the most common AM techniques being fused deposition modelling (FDM), selective laser sintering (SLS) and selective laser melting (SLM), electron beam machining (EBM) and more [53, 54]. Due to various applications and functions, some techniques are far better suited than others to achieve desired results where the resolution and fabrication quality dictate design trends. In other words, the development of metamaterials is closely linked to the advances in additive manufacturing technologies as illustrated in Figure 3.1.

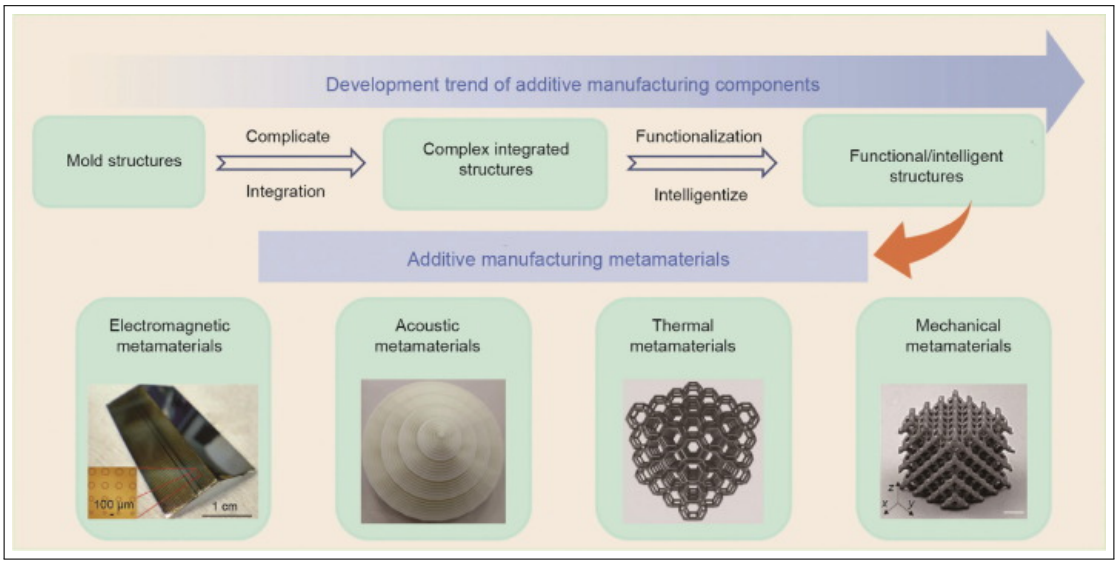

Figure 3.1: Relationship between development trends of AM components and AM metamaterials [54].

In the literature, multitude of AM techniques are used to fabricate 2D multistable systems, auxetic, chiral, pentamode as well as biomimetic metastructures [6, 55]. However, it was observed that 3D multistable structures are mainly fabricated using FDM or laser printers. In some cases, lattice 3D metastructures use unorthodox methods like laser cutting [44], water jet [47] or hot pressing [56].

Due to the inherent structure of metamaterials and their variety, UC size differs depending on the material type and functionality. It is evident, that the gap between macro- and micro scale metamaterials is present where most bistable UCs found in literature are more than 10 mm in size as it was shown in Table 2.1. A more comprehensive list of fabricated metamaterials span-

ning from the macro scale to the micro scale has been collated by TU Eindhoven researchers which describes all types of metamaterials like origami/kirigami, cubic lattices, sarrus linkage, miura-ori, bow-tie metamaterials. The paper indicates that metamaterial fabrication methods with decreasing cell size are ordered as: laser cutting, casting, 3D priting and 3D laser lithography for the smallest possible features [57]. For the characteristic length of a UC of 1-20 mm, casting and 3D printing are the most common techniques. In case of multistable 3D lattice metamaterials, examples at micro scales are very limited indicating that the challenges associated with scaling down are inherently linked to technological limitations. Hence, the proposed MECOMOS project is a potential solution for this issue.

The main objective of the MECOMOS project is to advance micro fabrication techniques for the 3D multi-scale, multi-material structures. The manufacture is proposed by first fabricating the sheets, using combinations of embossing and 2D&3D printing of sacrificial, structural and actuator materials, followed by sheet stacking to create a 3D structure [9]. On paper, this may appear relatively straightforward, however, key fabrication steps like forming, machining and joining must be considered to evaluate design feasibility at micro scale. Thus, to realise a 3D passive multistable system, this chapter will cover all necessary fabrication and assembly steps as well as their limitations. This includes modern techniques for thermoplastic polymer forming, methods of obtaining shape by laser machining and finally, joining/assembly techniques for micro multi-layer stacking.

3.1 Forming

The simplest and most common method for preparing multistable mechanical metamaterials are mould casting or 3D printing [13]. Both methods, especially 3D printing, are well documented, however, less known processes like thermoforming or hot embossing are emerging as potential fabrication method for multistable mechanical metamaterials. Plastics and thermoplastics in these fabrication processes are very common, however, more advanced thermoplastics like PEEK (Polyether-ether-ketone) are poorly covered. Although due to its mechanical and chemical properties, PEEK has been actively used in biomedical and aerospace fields. Despite that, not much is researched in mechanical metamaterial domain. In this section, current advancements of micro-thermoforming and micro-hot embossing techniques will be covered followed by recent fabrication success in PEEK forming by TU Delft research.

As defined, thermoforming is a process of plastic sheet extrusion where the sheet is heated to a temperature until it is soft and malleable [58]. In principle, the amorphous sheet of plastic is heated to a preselected forming temperature, called the glass transition temperature where it changes its mechanical properties from brittle, glassy state to ductile, rubbery state. Once heated, it is transported to a forming press where stretching onto or into the cool shaping mould takes place as shown in Figure 3.2 a). Most thermoplastics fall into the semicrystalline category, PEEK included, meaning that thermoforming window is very narrow making it a more difficult process where 20% variation in wall thickness results in 60% stiffness variation [58].

Contrary to thermoforming, during micro hot embossing a substrate is placed into the textured moulds which are then heated to the glass transition temperature of the material. As a result,

only texture and surface topology of the substrate is changed instead of the whole structure [59]. A major advantage of this fabrication method is capability of transferring micro- and even nano scale features onto the polymer substrate allowing more flexibility in lattice design and functionality. Compared to other forming methods like µ-injection moulding, hot embossing produces higher quality parts due to lower residual stresses and less shrinkage after embossing. Researchers presented current achievements in the industry where polymer foil sheets as thin as 50 µm were embossed with surface roughness within a few nm [60]. Variations of conventional hot embossing techniques are plate-to-roll (P2R), roll-to-plate (R2P) and roll-to-roll (R2R) where more advanced techniques like gas-pressurised hot embossing, ultrasonic hot embossing, laser-assisted hot embossing etc., are available depending on application [59, 60].

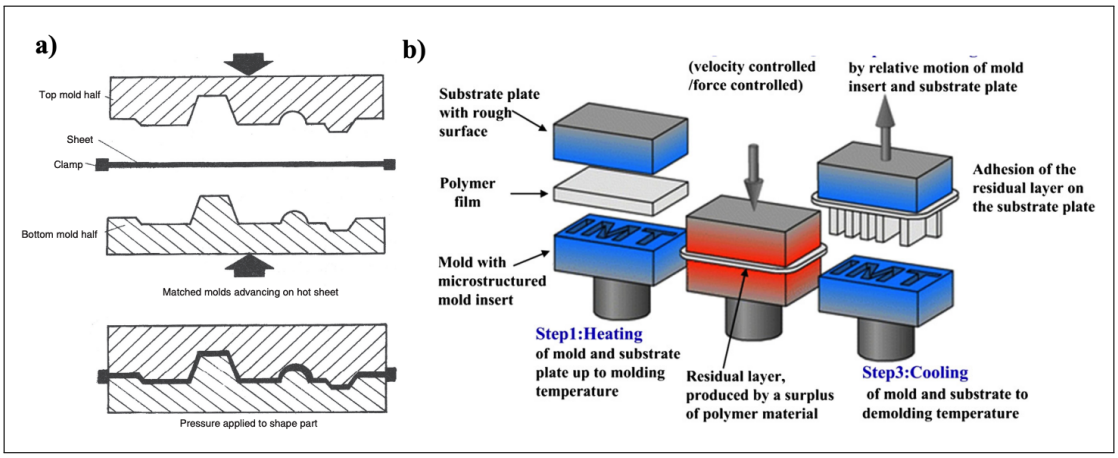

Figure 3.2: **a)** Schematic of matched mould thermoforming [58]. **b)** Schematic of a typical micro hot embossing [59].

Now, a more unique approach combining two forming methods, was developed by incorporating hot forming with a heating chamber [61]. This effectively combines benefits of both methods where high precision of hot embossing is incorporated with formation of the entire substrate as done in thermoforming. However, due to infancy stage of such research, the precision and accuracy were not the main goal but rather proving the concept of PEEK sheet moulding. Nevertheless, obtained results were promising for the future work.

Key factors influencing the quality and repeatability of PEEK sheets is the quality of 3D resin printed moulds and the hot forming process. Key variables influencing the mould output in resin printing were cleaning procedure, post-curing, and layer thickness. This resulted in resin moulds with the smallest features of $0.4 \times 0.4 \times 0.1$ mm. Different printing errors in small and big features were also affected by bleeding during the printing process and the edge rounding effects respectively which are closely linked to the printer and resin used. During the hot forming process of PEEK sheets, forming parameters proved to be highly forgiving resulting in high replication quality. It was further explored and found that no limitations concerning the shape or minimum size of the PEEK sheet features were present. The work concludes that high aspect ratio resin mould features are challenging to produce (excessively large and overly small), however, this can be mitigated with improved 3D printed, machined moulds or optimised mould fabrication process.

3.2 Laser machining

To create the shape of a bistable UC and achieve snap-through displacement at micro scale requires high precision and tolerance. Micro scale subtractive manufacturing (µSM) is a micromachining process which produces high resolution features and is used in many engineering industries. µSM encapsulates multiple techniques which can be distinguished into a few categories like micro-milling, micro electrical discharge machining (µEDM), laser beam machining, electron beam machining, focused ion-beam machining (FIB) and photo-chemical machining. In recent years utilisation of laser beam machining to obtain sub-cm feature resolution in polymers has gained a lot of attention in µSM domain. Working principle is described as focus of a high-powered focus beam to remove material by melting or vaporizing local area due to photon energy absorption. Compared to conventional methods like µCNC mills or other mechanical machining tools, laser machining is less expensive, more precise, fast, clean, contactless, flexible, not having tool wear, and produces less industrial effluents [62]. Quality of the cut is heavily dependent on the laser processing parameters, type and supplied power which sometimes requires a lot of tuning and optimization. This includes pulse duration, wavelength, pulse number, transition speed, material thermal conductivity, reflectivity coefficient and other parameters. High precision within 1 - 5 µm can be achieved with relatively high throughput compared to µEDM or FIB machining. The biggest drawback with laser beam machining is the heat affected zone (HAZ) and concentrated von-Misses stresses due to sharp temperature gradients during processing which subsequently causes local degradation in the cutting zone. Although new research of femto-second pulse lasers has shown significant improvements in HAZ control and surface quality, industrial challenges, setup difficulty and cost are limiting factors of such technological advancements [63].

3.3 Joining

Once individual sheets are made with unique UC shapes, they must be joined together by stacking layer-by-layer as defined by *MECOMOS* method. Joining is an essential operation for realisation of a functional product. It can be described as a temporary or permanent assembly between key components through mechanical, chemical or intermolecular adhesion. Depending on the application or function of the product, joining is distinguished into three main scales: macro-, micro- and nano-joining. Due to rapid technological advancements and miniaturization of parts in engineering fields, micro- and nano- joining has become more essential where it has gained vast popularity in fields lime electronics, microelectronics, medical equipment and precision engineering. The micro- and nano-joining definitions depend on definition of assembled units. That is, at least one of the dimensions, whether it being length, depth, height or width, is within 100 µm and 100 nm [64] where four distinct micro-joining strategies are shown in Table 3.1.
Micro-joining gained more and more attention as general size of characteristic length of metamaterials has decreased. Thus, micro-joining methods like solid state diffusion bonding, nanoparticle bonding, diffusion soldering/brazing, micro-welding and adhesive bonding processes have become significant due to their effectiveness in fabrication.

Table 3.1: Micro-joining techniques [65].

Solid State	Soldering/brazing	Fusion	Adhesive
Wire bonding	Diffusion bonding	Electron beam	Adhesive die attachment
Diffusion bonding	Flux less soldering	Laser beam	Flip-chip bonding
Friction stir bonding	Eutectic soldering/brazing	Resistance welding	Sealing
	Flip-chip bonding		

3.3.1 Solid state

Solid state micro joining process includes techniques like diffusion bonding, ultrasonic welding, friction welding, pressure welding and cold welding where main control parameters that determine quality of joints are bonding temperature, pressure, time and types of materials [65]. Solid state bonding process are associated with plastic deformation at material mating surface. Advantages of such method enables ability to join almost all types of metals, alloys, superalloys, ceramics, polymers, composites, and similar and dissimilar materials. In forge welding and cold welding approach, three bonding mechanisms such as contaminant displacement/interatomic bonding, decomposition of the interfacial structure and dissociation of retained oxides are included. To avoid oxidation, formation of voids, loss of alloying elements and additional contaminants during joining process, solid state diffusion is carried out in vacuum conditions or at inert gas pressurised environments [66].

Solid state welding processes require obligatory modifications in the set-up stage due to many problems such as pressure requirement, heat dissipation, complex geometry, materials variety, and tool manufacturing. To avoid these complications in friction stir welding (FSW), an insulating anvil, precise tool fabrication, and the use of high rotational speeds combined with low welding speeds are employed. In diffusion bonding, for example, the heating chamber of a furnace must be equipped with adequate systems for pressure application. It can also be noted that bond formation in solid-state diffusion is rather time consuming since it depends on applied pressure and temperature [65, 66].

3.3.2 Soldering and brazing

In micro joining, diffusion soldering and brazing are most commonly applied in cases where joining materials is challenging. Although both processes are inherently similar due to melting of a filler metal or alloy to bind the junction between two metals, they differ at operating temperatures required for joining. Brazing takes place at temperatures greater than $450°C$ whereas temperature for soldering is less than that. In addition, difference between these methods is evident during inter-metallic phase formation at application area. That is, intermetallic phase forms during diffusion soldering which is not observed in the case of brazing. Thus, diffusion micro brazing is mainly used in large scale production contrary to diffusion soldering, which is focused more towards smaller production volumes. These both micro-joining processes are very sensitive to multiple parameters during joining like interlayer thickness, interlayer composition, pressure, heating rate, joining temperature, isothermal hold time, and homogenizing heat treatment which requires fine tuning for successful results [65].

Out of two, brazing produces stronger and more reliable joints, however, due to higher melting temperatures, capillary forces drawing the molten filler metal into the joints are stronger. Thus, key driving property for high quality joints is wettability of brazing fillers [67]. Wettability indicates fluidic properties of the filler on the substrate surface as well as efficiency of molten filler penetration during the joining process. On the other hand, increased gaps between the joints need to account for filler fluidity, otherwise, low filler viscosity may result in a poor joint quality due to flow down. Brazing is also sensitive to cooling rate where joint characteristics such as hardness, ductility and strength are affected.

Two contemporary methods based on diffusion soldering process are laser soldering and flux soldering. With laser soldering, high power and high-density laser beam is used to melt the solder material which, in turn, fills the gaps, solidifies and creates the required joint. Noteworthy, laser is used to heat up a localised area and the solder to achieve necessary wettability but does not melt the joint surface. Conversely, flux soldering involves removal of the oxide layer of the metal for a reliable joint i.e., flux helps the removal of the oxide layer from the bonding surfaces and prevents further formation of the oxide layer at the clean bonding surfaces further facilitating localised heating of the joint [65].

3.3.3 Fusion bonding

Fusion bonding, as name suggests, fuses two materials together by the process of liquefying at the interface and solidifying to form a uniform weld. The fusion process requires controllable heat source and heat transportation method. There are multiple types of heat sources like electrical, chemical, photonic or magnetic. Electrical heat sources use electrodes to generate heat, chemical sources utilise gaseous fluids, photonic - lasers and magnetic sources induce heat through eddy currents. Most common micro-welding processes used for joining micro-devices are laser micro-welding, electron beam micro-welding, and resistance micro-welding as seen in Table 3.1.

Electron beam welding utilises acceleration of electrons under high voltage. Advantage of this technique is ability to join all electrically conductive materials despite dissimilar joining interfaces with low thermal distortion. This process converts kinetic energy of accelerated electrons into localised thermal energy upon impact at welded joint area. Such process is well suited for micron to -sub-milimeter range, however, is expensive energy-wise. High quality welds can be achieved due to vacuum working conditions. On the other hand, µ-electron beam joining technique is still relatively new with limited examples of working materials like thermoplastics or alloys as well as rectifying thermal distortions is yet to be studied [65].

In resistance micro-welding, electric current is passed through the interfaces of two electrically resistive materials. Due to physics of Joule's heat loss, heat induction occurs at the joint interface where with the pressure assistance, joint is produced. Several advantages of this method are that no filler material is required, can join dissimilar materials (similar to other fusion methods) and can produce very localized heat input for delicate parts of assemblies. It also possible to use gas tungsten arc welding or plasma welding to achieve high accuracy micro-spot welding, however, such techniques pose great control difficulties and thus, are rarely recommended [66].

3.3.4 Adhesive bonding

Sometimes joining materials via traditional methods like welding or soldering may not be the most efficient process where high precision or increased material sensitivity is concerned. Adhesive bonding is a joining method where adhesive layer is used to connect two similar or dissimilar materials like metals, ceramics, plastics and composites. This process does not change or alter material surfaces compared to traditional melting phenomena due to soldering. Advantages of such joining method are preferred when soft materials, films or material alike are joined. The quality of adhesive bond depends upon properties of both adhesive and substrate. That is, the substrate surface must be correctly prepared for adhesion to take place since wetting property determines the bonding quality [65]. Surface preparation involves removal of contaminants or surface alteration via chemical or mechanical ways. These are anodizing, degreasing, plasma treatment or abrasion, laser etching respectively. Furthermore, to achieve intimate contact between materials, mild pressure and correct adhesive dosage is required during the bonding process. Insufficient care in adhesive application may lead to cohesive or adhesive failures which occur inside adhesive layer or at the interface respectively. For mass distribution of adhesive substance, methods like pin transfer, stencil printing or spin coating are widely used. For more localised dispensing, auger pump, piston pump or jet dispensing are preferred.

This section concludes currently available micro scale fabrication methods found in the literature that are necessary to manufacture a 3D multistable metastructure using MECOMOS method. Currently available techniques for sheet moulding, precise laser machining and layer adhesion have been covered with their respective pros and cons. The following chapter will collate micro fabrication findings and draw conclusions for development and fabrication of such novel motion systems.

4 | Multistable system

As mentioned previously in Chapter 1, the MECOMOS method is a unique branch in metamaterial fabrication developed by TU Delft to precisely align optical components in high-tech machines. Previous chapters covered underlying physics in bistable UCs and multistable metamaterials as well as fabrication methods and techniques at microscale. In this section, all of these topics will be considered and compared against to establish feasibility in manufacturing 3D lattice sheet-based multistable metastructure. Factors like performance, effectiveness and limitations of the fabrication will be discussed. Lastly, conclusions will be derived regarding the final design.

4.1 Mechanics

From the perspective of mechanics of snap the through-bistability, regardless of the scale, micro-sized UCs demonstrate exact behaviour as macro-sized metamaterials as long as relative dimensions are maintained. That is, there is no geometrical limit for bistability since it is dictated by geometric parameters and relationships like t/h, h/l etc. which applies to any UC design. As discussed, stiffness difference in buckling element and support structure is crucial in maintaining an ideally symmetrical snap-through transition. That is, the support structure must be much stiffer and more rigid. The deterministic deformation required for precision applications can be controlled by varying stiffness of the buckling element or by adjusting dimensional characteristics. Furthermore, topology of the UC also impacts the performance of the structure where not only external but internal structure can influence total force required for snap-through as discussed in Chapter 2. Combining all of these various factors, Table 2.1 illustrated numerous examples of 3D multistable metastructures. Two distinct UC types were established: a pre-curved beam and a curved dome shell. Noteworthy, there are two types of curved dome shells where one is made as a "true" thin shell and the other by revolving pre-curved cosine beam. No publications were found where true spherical shell domes are used as a stacked multistable metamaterial and thus, revolved cosine beam is referred to as a dome shell in this literature review. Finally, the third type was also distinguished, however, due to their unique designs, they are difficult to categorise. Hence, focus is shifted towards beam and dome UCs.

The pre-curved beam and dome shell UCs have proven to have great stiffness, energy absorption and tunability characteristics. Despite that, depending on the specific requirements, one design may prove more appropriate over the other. Regardless of the wide application of bistable beams, certain limitations are unavoidable like failure at boundary constraints due to skew, low relative threshold forces, and asymmetric buckling. On the other hand, they are easier to fabricate and are relatively lightweight which is extremely important for space applications. It was observed that the dome shells UCs generally require more critical force F_{cr} to enter the second stable state (illustrated in Figure 4.1) as well as their multistable systems exhibit more pronounced hysteresis during the loading cycle. Moreover, it was analysed that the dome UC structures perform better than the the beam UC structures due to improved boundary conditions at the base achieving superior symmetric and smoother deformation. The most notable drawback of the cosine dome shell is the six time increased mass due to added material com-

pared to the single beam UC [49]. Thus, there are pros and cons to using either of the UC types which need further evaluation during the fabrication stage.

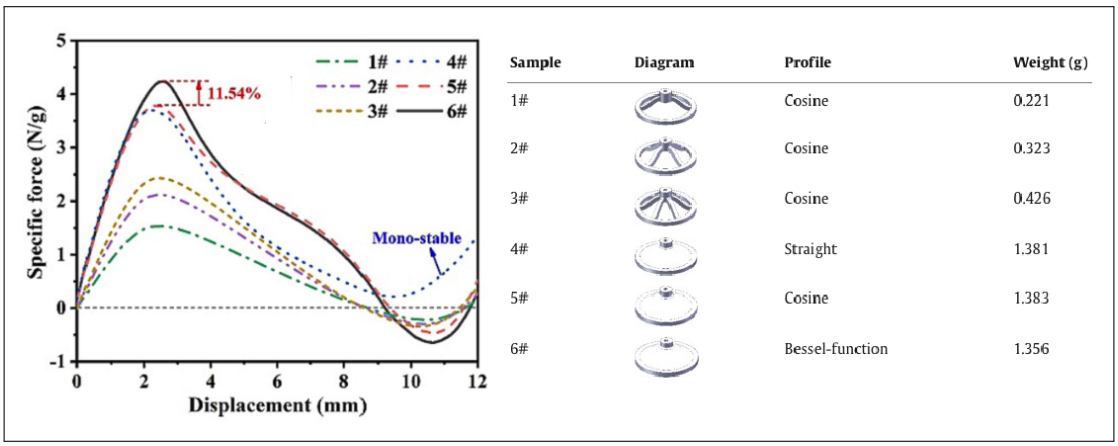

Sample	Diagram	Profile	Weight (g)
1#		Cosine	0.221
2#		Cosine	0.323
3#		Cosine	0.426
4#		Straight	1.381
5#		Cosine	1.383
6#		Bessel-function	1.356

Figure 4.1: Force-displacement plot of varying UCs under quasi-static loading, adapted [49].

Chapter 3 covered fabrication techniques at μm scale and how that is applied from mechanical metamaterial perspective. However, most of the information is tailored towards metastructures that are auxetic, chiral or ori- and kirigami based. Literature that presents difficulties in manufacturing bistable metastructures, unfortunately does not mention classical pre-curved beam UC architecture [68].

4.2 Development and fabrication

Considering the fabrication method of stacked metastructure, majority of surveyed examples are manufactured either using 3D printing or laser-based techniques (with a few exception as seen in Table 2.1). Indeed, using 3D printing greatly simplifies testing and demonstration of specific designs at a cost of scaling down. However, the challenge with conventional methods is limited to accuracy, precision, repeatability and surge in setup complexity with 3D printing techniques once scaled down. In addition, 3D printing associated constraints such as anisotropy, resolution limits, and build direction weakness are present. Thus, a new method of PEEK hot forming was introduced. As discussed previously, promising results were obtained indicating that micro-scale cells can be developed and subsequently, combined into multistable metastructures. A 4×4 mm PEEK sheet was formed with trapezoidal open geometry design demonstrating a multi-stable unit design as shown in Figure 4.2. Although the author of the paper did not explore any other shapes and geometries, a proof of concept was demonstrated. Nevertheless, despite necking along the edges, laser cut features were adequately replicated.

The key factor in achieving bistable cell is having a buckling beam segment and a rigid support on the edges which would enable satisfactory snap-through transition. Non-uniform thickness trapezoids were hot formed by adjusting Δx demonstrating viability for multi-stable behaviour [61]. However, more detailed analysis would be required to estimate stiffness variations to achieve tunable stacking. Multiple locations or even multiple layers may need to have varying stiffness to enable multistability. The highest risk associated with the pre-curved beam UC fabrication is maintaining a high-aspect ratio beams for adequate Q factor as forming such thin

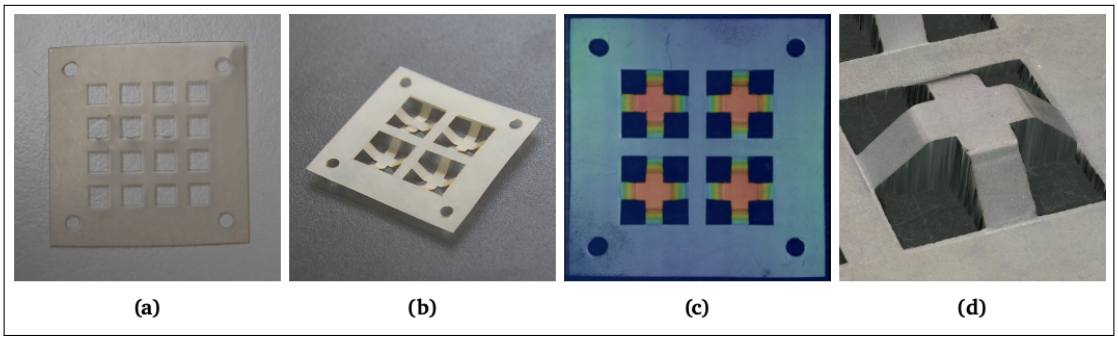

Figure 4.2: Unformed **(a)** and formed **(b)** laser-cut $4 \times 4mm$ substrate, **(c)** height map of the formed substrate, **(d)** microscope close-up of a UC [61].

elements may pose a great challenge. Regarding topological modifications, most of what was discussed in Chapter 2 can be implemented, however, an internal UC structure of the beam like internal lattice or hollow cross-section designs are beyond the capabilities of the current fabrication approach. Regarding dome shell formations, due to increased surface area, a passibility in variation of thickness must be carefully considered when forming to sustain uniform shape for symmetric snap-through. Finally, in previously covered deep domes, a novel boundary condition was observed where dome was connected to a square base, contrary to what can be expected for a circular shape. As per author's indication, such solution was employed for enhanced integration and connectivity between the domes, especially once they are stacked into a 3D multistable structure [31].

Micro-laser machining is a great option for fabricating UCs and required shapes yet, optimizing laser parameters is crucial. Most common challenge is avoiding formations of the HAZ and ensuring a high cutting zone/edge quality. New developments of femtosecond lasers have shown that thermal implications can almost be negligible, however, lack of robustness, user-friendliness and cost need to be considered. In the metamaterial fabrication laser µ-machining process is mostly confined within 2D shapes. In combination with computer-aided manufacturing (CAM) technologies, it has been used for fabrication of 2D auxetic patterns, kirigami-based auxetic rubber sheets, re-entrant auxetic polyimide films, auxetic stainless steel sheets and, less so, for multi-stable metastructures [6]. Thus, exploration of this fabrication method may open new horizons in the mechanical multistable metastructure fabrication domain.

Joining techniques of the thin PEEK substrate is a challenging task. The most appropriate micro-joining technique for the MECOMOS would be the fusion bonding or adhesive bonding. Previous research on fusion bonding, specifically the laser transmission welding, demonstrated effective and highly precise results of joining thin PEEK sheets at similar and dissimilar thicknesses. Despite that, such method had a several drawbacks like small fluence threshold, strict optimal weld requirements for $125\mu m$ sheets and challenge of maintaining the shape during the weld process [69]. Hence, more viable option for stacked construction can be adhesive bonding. Even though some articles in the literature have mentioned using strong glue to join multiple lattices or multi-material structures, no indication about the glue type, amounts and locations has been mentioned [35]. The most significant challenge with this method is application accuracy and, if photosensitive materials are used, optimal curing conditions. Below, key technical requirements are listed to achieve lattice multistable metastructure shown in Table 4.1. Thus,

Table 4.1: Key technical parameters required for stacking individual multistable layers.

Technical parameter	**Description**
Topology	Produce optimal UC design for bistable cells. Take into account sequential snap-through transition and adjust sheet design accordingly.
Surface Conditions	Ensure that the connecting surfaces can appropriately mate and are prepared for bonding by adjusting roughness and flatness
Bonding Quality	Apply right amounts of adhesive to local areas. Prepare right conditions for curing.
Orientation Control	Align and stack surfaces so that sequential multistability can be achieved. Reduce misalignment errors.
Environment	Clean fabrication and stacking room is required. Minimise dust and debris during assembly.

with such progress in micro fabrication of metamaterials, a solid ground is set for further development and research.

5 | Conclusions

In conclusion, this review explores state-of-the-art 3D multistable mechanical metamaterials and aims to answer the questions ***What geometric parameters determine multistablity of the metastructure?*** and ***How current micro fabrication techniques in relation to the MECOMOS affect design and mechanical performance of stacked multistable metastructures?*** To answer these questions, this review has been narrowed down to a specific type of mechanical metamaterials which are based on the bistable snap-through deformation. Following further classification, the most prospective UC designs are pre-curved beams and cosine dome shells since other designs are difficult to classify and are not well explored. Pre-curved beams and cosine dome shells possess multiple advantages and disadvantages where depending on the application, one can be preferred over the other. Nonetheless, pre-curved beam designs are widely covered in the scientific community due to its simplicity, lightweight and effectiveness whereas dome shells have emerged relatively recently providing more symmetric snap-through deformation and higher overall stiffness. Bistability mechanism of the UC is purely driven by geometric constraints where parameters like Q factor, h/l and t/l ratios, relative thickness t_2/t_1 and geometric similarity P are the most important. In addition, to achieve a deterministic collapse sequence, relative stiffness of each individual row needs to be tailored which, in turn, is driven by geometric parameters like beam thickness t and factor a_3. Unfortunately, it is difficult to draw any meaningful geometric parameters for the unique UC types due to their limited numbers in the literature.

Now, the literature review identifies multiple research gaps. Firstly, up to now research of multistable mechanical metamaterials was mostly focused from the perspective of energy dissipation by presenting a lot of unknowns in alternative applications like motion systems. This, evidently, aligns with the MECOMOS project, requiring novel designs for micro mechanical motion systems used in space applications. The gap can be associated with multiple restrictions of whom fabrication is the most crucial constraint. That is, in theory there are no limitations for scaling down, however, that is not the case once fabrication methods are considered. 3D printing strongly dominates in manufacturing of multistable metastructures. However, it becomes unfavourable once sub-centimetre designs are introduced. As seen in previous chapters, some of the illustrated examples are made in micro scale, however, fabrication complexity greatly increases making it less favourable. Secondly, repeatability of designs is a major concern where using conventional 3D printing methods can result in anisotropic prints, surface imperfections, poor tolerance control and necessary post-curing. The MECOMOS method aims to tackle these issues by combining currently available micro fabrication techniques to manufacture a high precision functional metamaterial structure. Third, to design a precision motion system, multiple DoF are required. This, however, is superficially explored as majority of tests are of a quasi-static nature resulting in a single DoF (compression or extension). Despite that, some papers have investigated multistable DoF concepts by providing potential insight for novel motion systems. This concludes the main findings of the literature review, highlighting the gaps in the current research and suggesting directions for developing a novel compact motion system using the MECOMOS method.

Bibliography

1. Valipour, A., Kargozarfard, M. H., Rakhshi, M., Yaghootian, A. & Sedighi, H. M. Metamaterials and their applications: An overview. EN. *Proceedings of the Institution of Mechanical Engineers, Part L: Journal of Materials: Design and Applications* **236,** 2171–2210 (2022).
2. Xianglong, Y., Ji, Z., Haiyi, L., Zhengyi, J. & Lingling, W. Mechanical metamaterials associated with stiffness, rigidity and compressibility: A brief review. *Progress in Materials Science* **94,** 114–173 (2018).
3. Andrew, M., Fadel, G. M. & Gang, L. Design for energy absorption using snap-through bistable metamaterials. *Mechanics Based Design of Structures and Machines* **51,** 1368–1386 (2023).
4. Emilio, B., Mario, S. & Luca, P. Mechanical metamaterials: a state of the art. *Mathematics and Mechanics of Solids* **24,** 212–234 (2019).
5. Pendry, J. B. Negative Refraction Makes a Perfect Lens. en. *Physical Review Letters* **85,** 3966–3969 (2000).
6. Pyo, S. & Park, K. Mechanical Metamaterials for Sensor and Actuator Applications. en. *International Journal of Precision Engineering and Manufacturing-Green Technology* **11,** 291–320 (2024).
7. Tan, X. *et al.* Negative stiffness mechanical metamaterials: a review. en. *Smart Materials and Structures* **34,** 013001 (2025).
8. Yan, S., Wu, L., Wen, Y., Sun, J. & Zhou, J. Snap-through instability in mechanical metamaterials. en. *Responsive Materials* **3,** e20240035 (2025).
9. Herder, J. *et al. Mechanical metamaterials for compact motion systems (MECOMOS)* (ed TU Delft)
10. Bertoldi, K., Vitelli, V., Christensen, J. & Van Hecke, M. Flexible mechanical metamaterials. en. *Nature Reviews Materials* **2,** 17066 (2017).
11. Chi, Y. *et al.* Bistable and Multistable Actuators for Soft Robots: Structures, Materials, and Functionalities. en. *Advanced Materials* **34,** 2110384 (2022).
12. Jiao, P., Mueller, J., Raney, J. R., Zheng, X. (& Alavi, A. H. Mechanical metamaterials and beyond. en. *Nature Communications* **14,** 6004 (2023).
13. Xu, R. *et al.* The design, manufacture and application of multistable mechanical metamaterials-a state-of-the-art review. en. *International Journal of Extreme Manufacturing* **5,** 042013 (2023).
14. Zhang, C. *et al.* A review on reprogrammable bistable structures. en. *Smart Materials and Structures* **33,** 093001 (2024).
15. Qiu, J., Lang, J. & Slocum, A. A Curved-Beam Bistable Mechanism. en. *Journal of Microelectromechanical Systems* **13,** 137–146 (2004).
16. Shan, S. *et al.* Multistable Architected Materials for Trapping Elastic Strain Energy. en. *Advanced Materials* **27,** 4296–4301 (2015).
17. Faber, J. A., Udani, J. P., Riley, K. S., Studart, A. R. & Arrieta, A. F. Dome-Patterned Metamaterial Sheets. en. *Advanced Science* **7,** 2001955 (2020).
18. Liu, M., Domino, L., Dupont de Dinechin, I., Taffetani, M. & Vella, D. Snap-induced morphing: From a single bistable shell to the origin of shape bifurcation in interacting shells. *Journal of the Mechanics and Physics of Solids* **170,** 105116 (2023).
19. Rafsanjani, A. & Bertoldi, K. Buckling-Induced Kirigami. en. *Physical Review Letters* **118,** 084301 (2017).
20. Li, Z., Li, X., Zhou, Y., Mo, Z. & Li, J. Bistability of the square deep dome and energy dissipation of its multistable metamaterials. en. *Thin-Walled Structures* **216,** 113708 (2025).
21. Yang, H. & Ma, L. Multi-stable mechanical metamaterials with shape-reconfiguration and zero Poisson's ratio. en. *Materials & Design* **152,** 181–190 (2018).
22. Hang, Y. & Li, M. Multi-stable mechanical metamaterials by elastic buckling instability. en. *Journal of Materials Science* **54,** 3509–3526 (2019).
23. Zhang, Y., Tichem, M. & van Keulen, F. A novel design of multi-stable metastructures for energy dissipation. *Materials & Design* **212,** 110234 (2021).

24. Ha, C. S., Lakes, R. S. & Plesha, M. E. Design, fabrication, and analysis of lattice exhibiting energy absorption via snap-through behavior. en. *Materials & Design* **141,** 426–437 (2018).

25. Baocai, C. *et al.* Novel multifunctional negative stiffness mechanical metamaterial structure: Tailored functions of multi-stable and compressive mono-stable. *Composites Part B: Engineering* **204,** 108501 (2021).

26. Hua, J., Lei, H., Gao, C.-F., Guo, X. & Fang, D. Parameters analysis and optimization of a typical multistable mechanical metamaterial. en. *Extreme Mechanics Letters* **35,** 100640 (2020).

27. Ju, X., Li, S., Zhang, Y., Wu, P. & Li, Y. Design of multi-stable metamaterial cell with improved and programmable energy trapping ability based on frame reinforced curved beams. en. *Thin-Walled Structures* **202,** 112120 (2024).

28. Mehreganian, N., Razi, S., Fallah, A. S. & Sareh, P. Mechanical performance of negative-stiffness multistable bi-material composites. en. *Acta Mechanica* (2024).

29. Zhang, Y., Tichem, M. & van Keulen, F. Concept and design of a metastructure-based multi-stable surface. *Extreme Mechanics Letters* **51,** 101553 (2022).

30. Tan, X. *et al.* Effect of beam configuration on its multistable and negative stiffness properties. en. *Composite Structures* **286,** 115308 (2022).

31. Li, Z. *et al.* Mechanical response of a novel square dome shell with bistable behavior: Improved analytical method and empirical model. *Thin-Walled Structures* **198,** 111722 (2024).

32. Alturki, M. & Burgueño, R. Multistable Cosine-Curved Dome System for Elastic Energy Dissipation. en. *Journal of Applied Mechanics* **86,** 091002 (2019).

33. Tan, X. *et al.* Bioinspired Flexible and Programmable Negative Stiffness Mechanical Metamaterials. en. *Advanced Intelligent Systems* **5,** 2200400 (2023).

34. Che, K., Yuan, C., Wu, J., Jerry Qi, H. & Meaud, J. Three-Dimensional-Printed Multistable Mechanical Metamaterials With a Deterministic Deformation Sequence. en. *Journal of Applied Mechanics* **84,** 011004 (2017).

35. Yang, H. & Ma, L. 1D to 3D multi-stable architected materials with zero Poisson's ratio and controllable thermal expansion. en. *Materials & Design* **188,** 108430 (2020).

36. Jian, H., Hongshuai, L., Cun-Fa, G. & Daining, F. A Novel Design of Multistable Metastructure With Nonuniform Cross Section. *Journal of Applied Mechanics* **89** (2022).

37. Liang, K. *et al.* Programmable and multistable metamaterials made of precisely tailored bistable cells. en. *Materials & Design* **227,** 111810 (2023).

38. Hou, X., Sheng, T., Xie, F. & Deng, Z. Mechanical logic gate design based on multi-stable metamaterial with multi-step deformation. en. *Composite Structures* **335,** 118001 (2024).

39. Chen, H.-T., Taylor, A. J. & Yu, N. A review of metasurfaces: physics and applications. en. *Reports on Progress in Physics* **79,** 076401 (2016).

40. Hu, J., Bandyopadhyay, S., Liu, Y.-h. & Shao, L.-y. A Review on Metasurface: From Principle to Smart Metadevices. en. *Frontiers in Physics* **8,** 586087 (2021).

41. Frédéric, A., Tarantino, Gabriella, M. & Daniel, L. Mechanical behavior of embedded bistable dome shell with tunable energy barrier asymmetry. *International Journal of Mechanical Sciences* **263,** 108762 (2024).

42. Udani, J. P. & Arrieta, A. F. Programmable mechanical metastructures from locally bistable domes. *Extreme Mechanics Letters* **42,** 101081 (2021).

43. Tobias, F., Claudio, F., Muamer, K., Peter, G. & Martin, W. Tailored Buckling Microlattices as Reusable Light-Weight Shock Absorbers. *Advanced Materials* **28,** 5865–5870 (2016).

44. Zhang, Y., Wang, Q., Tichem, M. & Van Keulen, F. Design and characterization of multi-stable mechanical metastructures with level and tilted stable configurations. en. *Extreme Mechanics Letters* **34,** 100593 (2020).

45. Jian, H., Yuan, Z. & Qing, C. C. Design and analysis of a tunable multistable mechanical metamaterial. *International Journal of Mechanical Sciences* **272,** 109170 (2024).

46. Yang, H. & Ma, L. 1D and 2D snapping mechanical metamaterials with cylindrical topology. en. *International Journal of Solids and Structures* **204-205,** 220–232 (2020).

47. Tan, X. *et al.* Reusable metamaterial via inelastic instability for energy absorption. en. *International Journal of Mechanical Sciences* **155,** 509–517 (2019).

48. Wei, Z., Wu, Y., Lai, H. & Qian, J. Compression-Twist Coupling Mechanical Metamaterials with Programmed Bistability. en. *Acta Mechanica Solida Sinica* (2025).

49. Dong, Y., Yu, T. & Zhang, Z. Design and mechanical analysis of 3D negative-stiffness curved domes with Bessel-functional profile. en. *Composite Structures* **304,** 116422 (2023).

50. Shi, J., Mofatteh, H., Mirabolghasemi, A., Desharnais, G. & Akbarzadeh, A. Programmable Multistable Perforated Shellular. en. *Advanced Materials* **33,** 2102423 (2021).

51. Qin, Q. *et al.* Hierarchical negative stiffness mechanical metamaterials. en. *Smart Materials and Structures* **34,** 065008 (2025).

52. Xu, R., He, Y., Li, X., Lu, M. & Chen, Y. Snap-fit mechanical metamaterials. en. *Applied Materials Today* **30,** 101714 (2023).

53. Zadpoor, A. A., Mirzaali, M. J., Valdevit, L. & Hopkins, J. B. Design, material, function, and fabrication of metamaterials. *APL Materials* **11,** 020401 (2023).

54. Song, B., Zhang, S., Zhang, L. & Shi, Y. Development Trends and Challenges of Additive Manufacturing Metamaterials. en. *Engineering* **44,** 2–6 (2025).

55. Yuan, X. *et al.* Recent progress in the design and fabrication of multifunctional structures based on metamaterials. en. *Current Opinion in Solid State and Materials Science* **25,** 100883 (2021).

56. Chen, S. *et al.* Continuous carbon fiber reinforced composite negative stiffness mechanical metamaterial for recoverable energy absorption. *Composite Structures* **288,** 115411 (2022).

57. McClintock, H. D. *et al.* A Fabrication Strategy for Reconfigurable Millimeter-Scale Metamaterials. en. *Advanced Functional Materials* **31** (2021).

58. Throne, J. en. in *Applied Plastics Engineering Handbook* 449–480 (Elsevier, 2024).

59. Peng, L., Deng, Y., Yi, P. & Lai, X. Micro hot embossing of thermoplastic polymers: a review. en. *Journal of Micromechanics and Microengineering* **24,** 013001 (2014).

60. Deshmukh, S. S. & Goswami, A. Recent developments in hot embossing – a review. en. *Materials and Manufacturing Processes* **36,** 501–543 (2021).

61. Rings, M. *Microscale Hot Forming of PEEK* (ed TU Delft)

62. Juang, Y.-J. & Chiu, Y.-J. Fabrication of Polymer Microfluidics: An Overview. en. *Polymers* **14,** 2028 (2022).

63. Al Javed, M. O. & Bin Rashid, A. Laser-assisted micromachining techniques: an overview of principles, processes, and applications. en. *Advances in Materials and Processing Technologies* **11,** 1583–1626 (2025).

64. Zhou, Y. N. *Microjoining and Nanojoining* en (Elsevier, 2008).

65. Choudhury, M. R. & Debnath, K. in *Joining Processes for Dissimilar and Advanced Materials* (eds Rakesh, P. & Davim, J. P.) 209–239 (Woodhead Publishing, 2022).

66. Mehta, K. in *Advanced Manufacturing Technologies: Modern Machining, Advanced Joining, Sustainable Manufacturing* (ed Gupta, K.) 101–136 (Springer International Publishing, Cham, 2017).

67. Ahn, B. Recent Advances in Brazing Fillers for Joining of Dissimilar Materials. en. *Metals* **11,** 1037 (2021).

68. Askari, M. *et al.* Additive manufacturing of metamaterials: A review. en. *Additive Manufacturing* **36,** 101562 (2020).

69. Dijkman, W. *Laser Transmission Welding of thin PEEK films* (ed TU Delft)